Susceptibility-Guided Landslide Detection Using Fully Convolutional Neural Network

Yangyang Chen , Dongping Ming , *Member, IEEE*, Junchuan Yu, Lu Xu, Yanni Ma, Yan Li, Xiao Ling , and Yueqin Zhu

Abstract—**Automatic landslide detection based on very high spatial resolution remote sensing images is crucial for disaster prevention and mitigation applications. With the rapid development of deep-learning techniques, state-of-the-art semantic segmentation methods based on fully convolutional network (FCNN) have achieved outstanding performance in the landslide detection task. However, most of the existing articles only utilize visual features. Even if the advanced FCNN models are applied, there is still a certain amount of falsely detected and miss detected landslides. In this article, we innovatively introduce landslide susceptibility as prior knowledge and propose an innovative susceptibility-guided landslide detection method based on FCNN (SG-FCNN) to detect landslides from single temporal images. In addition, an unsupervised change detection method based on the mean changing magnitude of objects (MCMO) is further proposed and integrated with the SG-FCNN to detect newly occurred landslides from bitemporal images. The effectiveness of the proposed SG-FCNN and MCMO has been tested in Lantau Island, Hong Kong. The experimental results show that the SG-FCNN can significantly reduce the amount of falsely detected and miss detected landslides compared with the FCNN. It can conclude that applying landslide susceptibility as prior knowledge is much more effective than using visual features only, which introduces a new methodology of landslide detection and lifts the detection performance to a new level.**

Index Terms—**Convolutional neural network (CNN), landslide detection, landslide susceptibility mapping, Lantau Island, remote sensing.**

Yangyang Chen and Junchuan Yu are with the China Aero Geophysical Survey and Remote Sensing Center for Natural Resources, Beijing 100083, China (e-mail: jimmyxiyangyang@hotmail.com; yujunchuan@mail.cgs.gov.cn).

Dongping Ming is with the School of Information Engineering, China University of Geosciences, Beijing 100083, China, and also with the Polytechnic Center for Natural Resources Big-data, Ministry of Natural Resources of China, Beijing 100036, China (e-mail: mingdp@cugb.edu.cn).

Lu Xu, Yan Li, and Xiao Ling are with the School of Information Engineering, China University of Geosciences, Beijing 100083, China (e-mail: xlirs@cugb.edu.cn; liyanturbo@163.com; lingx0527@163.com).

Yanni Ma is with the China Aero Geophysical Survey and Remote Sensing Center for Natural Resources, Beijing 100083, China, and also with the School of Information Engineering, China University of Geosciences, Beijing 100083, China (e-mail: mayanni@mail.cgs.gov.cn).

Yueqin Zhu is with the National Institute of Natural Hazards, Ministry of Emergency Management, Beijing 100085, China (e-mail: yueqinzhu@163.com).

Digital Object Identifier 10.1109/JSTARS.2022.3233043

I. INTRODUCTION

SEASONAL torrential rainfall triggers vast landslides on the southeast coast of China every year, especially in mountainous terrains [1]. It is worth noting that with the rapid growth of urbanization and city expansion, the mountainous area once inhospitable has gradually changed into urban infrastructures. Therefore, landslide occurrence has posed an increasing threat to lives and property on the southeast coast of China in recent years. Taking Hong Kong Special Administration Region as an example, two fatalities were reported, and more than a hundred municipal roads were damaged or closed as a result of a landslide triggered by the rainstorm on 7th June 2008 [2]. To alleviate the negative impact of landslides and landslide-induced geohazards, industry and academia need to conduct in-depth research on landslide monitoring, susceptibility analysis, and early warning [3], [4].

Landslide inventories are the basis for carrying out the research mentioned above [4], [5] and can be obtained via landslide detection [6]. Therefore, it is vital to detect landslides precisely, quickly, and automatically [7]. In the early stages, landslide detection mainly relied on geological field survey [8]. Field survey can get highly reliable landslide information, but it is labor intensive [9] and can only be applied on a site-specific or local scale [4]. With the rapid development of satellite and sensor techniques since the 1970s, remote sensing products have been widely applied in the geoscience field [10], making it possible to detect landslides on a regional scale. Initially, remote-sensing-based landslide detection primarily relied on visual interpretations performed by geological experts [11]. In the 21st century, the launch of Google Earth and the emergence of open-source data have made it much easier to acquire remote sensing products with different sources and modalities [12], [13]. Although the promotion of remote sensing products improves the efficiency of landslide detection, visual interpretation still requires a considerable amount of human consumption [6], which leads to undesirable detection efficiency on a regional scale [14]. Besides, visual interpretation based on expertise and experience is subjective [11], [15]. Hence, visual interpretation failed to satisfy the demand for rapid landslide detection on a regional scale [4].

With advances in computer hardware and pattern recognition techniques, the accuracy of computer vision algorithms gradually approaches visual interpretation in various domains, which also benefits landslide detection. Remote-sensing-based

landslide detection is now moving from visual interpretation toward automatic interpretation [16], among which machine learning (ML)-based methods are the most representative. By extracting and utilizing low-level features of remote sensing images, various traditional ML models, such as maximum likelihood [17], support vector machine (SVM) [18], [19], and random forest (RF) [20], have raised the efficiency of landslide detection with acceptable accuracy. The spatial resolution of remote sensing images has significantly increased over the last few decades. However, very high spatial resolution (VHR) remote sensing images suffer severe interclass similarity [21], [22]. For example, muddy tracks and dry riverbanks are indistinguishable from landslides because they share similar spectral features. Interclass similarity poses a conundrum for traditional ML algorithms, and it is challenging to obtain ideal landslide detection results by utilizing only low-level features. Mining the high-level features of VHR remote sensing images is the key to improving detection accuracy and reliability.

After entering the new century, numerous powerful deep-learning (DL) models have been launched and put to scientific use. As the most mature and widely applied DL model, the convolutional neural network (CNN) has exceptional advantages in high-level feature extraction and representation [23], which makes up for the defects of traditional ML models [24]. CNN has now been widely used in the geoscience domain, such as scene classification [25], land-cover classification [26], [27], change detection [28], [29], and ground target detection [30]. In recent years, many scholars have applied CNN in landslide-related domains, such as landslide susceptibility mapping [31], [32], landslide deformation prediction [33], [34], and especially landslide detection. There are mainly two types of CNN-based landslide detection models: Patch-based CNN (PBCNN) and fully CNN (FCNN) [35].

Yu et al. [36] first introduced the PBCNN and region growth algorithm to detect landslides. Ghorbanzadeh et al. [37] applied PBCNN to detect landslides in Nepal from Rapid Eye images and has proved that the PBCNN outperforms traditional ML methods, including SVM, RF, and multilayer perceptron. Sameen and Pradhan [38] utilized the PBCNN with advanced residual blocks to detect landslides in Malaysia's Cameron highlands based on spectral features and topographical information derived from remote sensing products. Ji et al. [39] introduced the three-dimensional attention-boosted PBCNN model to detect landslides in Zhijin County, China, and achieved higher detection accuracy than other recent attention-based models. Although the PBCNN has made significant progress in the automatic intelligent detection of landslides, defects still exist. The principle of the PBCNN is to classify each pixel one by one, whose detection results will suffer from salt–pepper noise. In addition, for each pixel, a square image patch is clipped and fed into CNN for classification, which leads to extremely low efficiency and a heavy computational burden [26], thus limiting the efficiency of the PBCNN for detecting landslides on a regional scale.

The FCNN can generate pixelwise detection results at once [40], not predicting only the central pixel of the input image patch. Therefore, the FCNN can avoid the shortage of the PBCNN effectively and has drawn the attention of an increasing number of scholars. Meena et al. [41] compared the detection performance of U-Net, SVM, K-nearest neighbor, and RF in the Rasuwa district, Nepal. The U-Net achieved higher accuracy than other traditional ML models. Prakash et al. [42] modified U-Net using ResNet34 as the backbone and achieved better performance than pixel-based and object-based ML methods in Douglas County, USA. Liu et al. [43] modified U-Net by adding a residual learning unit and used it to improve the accuracy of postearthquake landslide detection in Jiuzhaigou, China. Braganolo et al. [40] utilized U-Net and the compound loss function to detect landslide scars from Landsat 8 images, and the result outperformed RF and the PBCNN. Ghorbanzadeh et al. [44] proposed an object-based image analysis (OBIA)-based ResU-Net to detect landslides in east Iburi, Japan, which achieved 22% higher intersection over union (IoU) than the original ResU-Net. Liu et al. [45] proposed an improved Mask R-CNN models for landslide detection in Jiuzhaigou, China, and achieved satisfactory accuracy with precision, recall, and overall accuracy (OA) of 95.8%, 93.1%, and 94.7%, respectively.

To date, scholars have been trying to apply advanced DL models to landslide detection, and the results show that DL models are superior to traditional ML models, especially the FCNN. However, since landslides are indistinguishable from some land cover features, false and miss detection still exist. One reason is the lack of datasets containing vast landslide samples with all kinds of features combined with the negative samples. Although adopting a data augmentation strategy can expand small datasets to a certain extent, detection results are still less than satisfactory.

Introducing auxiliary information is a promising strategy to improve landslides' detection accuracy further. Some researchers [16], [42], [46], [47], [48], [49], [50] fed remote sensing images and auxiliary information, such as elevation, aspect, land cover, and normalized difference vegetation index (NDVI) into CNN. It allows CNN to explore richer high-level features, especially the connection between landslide occurrence and surrounding environmental conditions, achieving higher detection accuracy. However, the auxiliary information is indispensable for training and testing regions. Besides, accurate geometric registration of different auxiliary information layers and correlated remote sensing images are also necessary. Meanwhile, the structure of the classical CNN needs to be redesigned carefully. Applying auxiliary information to the postprocessing of landslide detection results is another solution. For example, Shi et al. [51] used a binary mask operation to optimize landslide detection results based on road vectors, building vectors, and slope maps. The results showed that the precision and F1-score were substantially improved. However, the selection of auxiliary information and the determination of corresponding thresholds are often subjective. In addition, applying a specific type of auxiliary information is unreasonable. For instance, a binary mask operation may mistakenly remove detected landslides that crossed the road.

The landslide detection methods reviewed above are based on single temporal images and are feasible for generating the initial version of the landslide inventory. In actual applications,
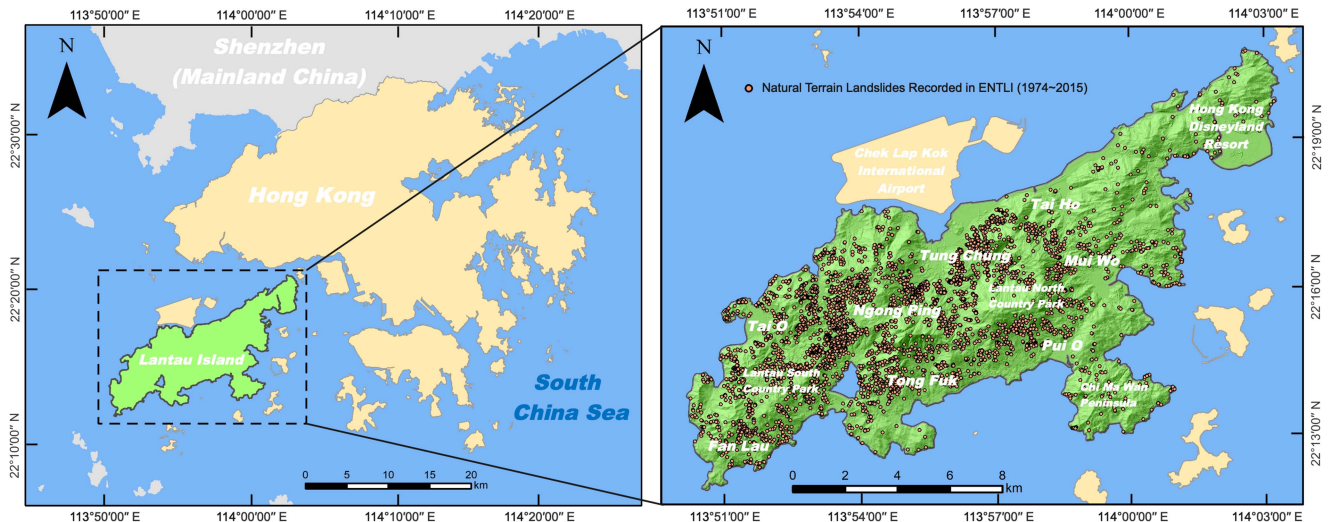
Fig. 1.   Location of Lantau Island.

detecting newly occurred landslides is equally essential [6]. With the help of bitemporal (postlandslide and prelandslide) images, the boundaries and occurrence time of newly occurred landslides can be obtained precisely [52]. Some researchers have recently applied the FCNN to detect newly occurred landslides. Stacking the postlandslide and prelandslide images and feeding it into the FCNN is the most widely applied strategy. However, the spectral difference of bitemporal images extracted by shallow layers may not represent semantic change and mistakenly propagate to deep layers, leading to false detection [53]. Shi et al. [51] first used the FCNN to detect landslides from postlandslide and preland-slide images, respectively. The newly occurred landslides were detected by utilizing the change detection technique based on OBIA, which outperformed unsupervised change detection methods based on the changing magnitude image (CMI) and all CNN-based rivals. Nevertheless, for all supervised methods, including the FCNN, detecting newly occurred landslides from bitemporal images require a much larger amount of labor on sample labeling than detecting landslides from single-temporal images, leading to lower processing efficiency.

To address the abovementioned issues, we propose a novel susceptibility-guided landslide detection method based on FCNN (SG-FCNN). Specifically, the landslide susceptibility map generated by the state-of-the-art CNN model is introduced as prior knowledge, which guides the FCNN to detect landslides from single-temporal remote sensing images. The landslide susceptibility map can provide the spatial probability of landslide occurrence in the near future [54], [55], which is obtained based on the analysis of landslide-related auxiliary information (also known as landslide predisposing factors). To the best of our knowledge, this is the first time that landslide susceptibility has been introduced as prior knowledge to guide the detection of landslides. Additionally, an unsupervised change detection method based on the mean changing magnitude of objects (MCMO) is proposed and jointly used with the proposed SG-FCNN, which expands the application field of the proposed SG-FCNN to the detection of newly occurred landslides from

bitemporal remote sensing images. It is also the first time that the unsupervised change detection method has been integrated with the FCNN to detect newly occurred landslides from bitemporal images.

This article is organized as follows. Section II introduces the study area. Section III presents an in-depth description of the proposed methods. Section IV shows the experimental details and results. Sections V and VI provide the discussion and conclusion, respectively.

II. STUDY AREA

In this article, Lantau Island, Hong Kong (shown in Fig. 1), which is situated on the southeast coast of China, is selected as the study area. As the largest outlying island in Hong Kong [56], Lantau Island is dominated by mountainous terrain and composed of volcanic rock and granite.

There are three reasons for selecting Lantau Island as the study area. First, Lantau Island has a subtropical monsoon climate with 2200 mm of average annual rainfall and frequent torrential rainfall, which triggers a vast number of landslides every year. Especially in June 2008, a record-breaking rainstorm triggered 2610 landslides (shown in Fig. 2), causing havoc and two fatalities on Lantau Island [57]. The types of natural terrain landslides on Lantau Island include debris flows, rockfalls, and slumps, among which debris flows appear most frequently [58]. Second, with the expansion of urban areas, an increasing number of infrastructures and landmarks have been built on Lantau Island over the past decades. Most of them are densely pop-ulated, such as Chek Lap Kok International Airport, Hong Kong Disneyland Resort, Tung Chung New Town, Discovery Bay, and Ngong Ping. Therefore, landslide prevention and mitigation on Lantau Island is crucial for Hong Kong authorities. Third, to carry out landslide-related applications and research, the Civil Engineering and Development Department of Hong Kong established the Enhanced Natural Terrain Landslide Inventory (ENTLI) based on annually updated digital aerial photos (DAPs)
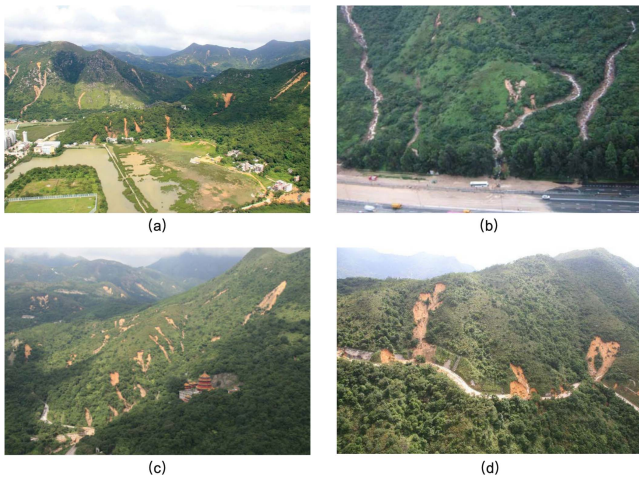
Fig. 2. Landslides triggered by the rainstorm in June 2008 [2]. (a) Nam Chung Tsuen, Tai O. (b) North Lantau highway. (c) Keung Shan Kwum Yum Temple. (d) Sham Wat road.

via visual interpretation by experts [59]. The latest version of the ENTLI contains the crowns and trails of 5340 landslides covered from 1974 to 2015 on Lantau Island. Related DAPs are purchasable on the Hong Kong Map Service 2.0 website (https://www.hkmapservice.gov.hk). Given the above, Lantau Island is an ideal study area for landslide detection.

III. METHODOLOGY

This article proposed the SG-FCNN to detect landslides on Lantau Island in 2008. Fig. 3 presents the detailed workflow. The general outline is divided into landslide susceptibility mapping and landslide detection.

For landslide susceptibility mapping, a series of landslide-related predisposing factors were first collected. Afterward, a state-of-the-art DL-based landslide susceptibility model, the ensemble model based on channel-expanded pretrained CNN and RF (CPCNN-RF) [31], was trained based on the predisposing factor layers and the ENTLI (from 1994 to 2007). Finally, the trained CPCNN-RF was applied to map the landslide susceptibility of Lantau Island. The generated landslide susceptibility map can be used to predict landslide occurrence after 2007. The methodology of the CPCNN-RF and the landslide susceptibility mapping process in Lantau Island have been detailed in [31]. Therefore, this article will not go into detail.

For landslide detection, there were two missions in this article: 1) detecting all landslides from single-temporal aerial images acquired in 2008, which includes historical landslides before 2008 and newly occurred landslides in 2008. 2) Detecting newly occurred landslides in 2008 from bitemporal aerial images acquired in 2007 and 2008. The related data were collected first, including the ENTLI (from 1994 to 2008) and the DAPs collected in 2007 and 2008. Then, landslide polygons were delineated by taking the record in the ENTLI (from 1994 to 2008) as referees, and an augmented training dataset along with DAPs (2008) was produced. After that, all landslides (including historical and newly occurred landslides) in DAPs (2008) were

detected by the proposed MobileU-Net under the guidance of landslide susceptibility. The boundaries of detected landslides were then optimized by the dense conditional random field (Dense CRF). Finally, to detect newly occurred landslides in 2008, bitemporal DAPs and the proposed MCMO were used to identify and remove historical landslides from the detection results of all landslides.

A. Data Collection and Preprocessing

1) Digital Aerial Photos: As shown in Fig. 4, a subset region of central Lantau Island was selected as the study area. Two testing regions are highlighted with red and green boundaries, and the other remaining areas are training regions. Six scenes of DAPs taken by the Geotechnical Engineering Office were purchased and applied, four of which (Photo numbers: CW82126, CW82130, CW82134, and CW82147) covered the whole study area were acquired in November 2008. The other two scenes (Photo numbers: CW79890 and CW79894) covered two testing regions were acquired in November 2007. All applied DAPs are digitized RGB aerial photographic films with a spatial resolution of 0.5 m, which were acquired by a Zeiss RMK TOP 15 aerial survey camera at a flying height of 8000 ft.

The data preprocessing of the DAPs was carried out in ENVI 5.1, including rational polynomial coefficient (RPC) generation, orthorectification, mosaicking, bitemporal image registration, and relative radiometric correction. First, 208 ground control points for exterior orientation were selected using Google Earth Pro. Based on which RPCs were generated as a reference to the calibration certificate. After that, orthorectification was conducted based on prepared RPCs and digital terrain model with a spatial resolution of 5 m. Then, the seamless mosaic technique was adopted to stitch the four scenes of the 2008 DAPs into a single image. Finally, the automatic histogram matching technique was applied for relative radiometric correcting of the bitemporal DAPs.

2) Training Dataset: The proposed SG-FCNN is based on semantic segmentation, and a pixelwise labeled reference map is required. The ENTLI only records landslide crowns and trails instead of the boundaries and cannot be directly used as a label for semantic segmentation. Therefore, landslide boundaries in the training regions were visually delineated as polygons by reference to the DAPs (2008) and the ENTLI (from 1994 to 2008). In the training regions, 672 landslide polygons were drawn and rasterized into binary label maps.

To make up the training dataset, DAPs and their corresponding binary label maps were clipped into square patches with a size of 416×416. In most previous articles, the grid-clipping strategy is performed to generate square patches. However, considering the arear of training regions are relatively small and the complexity of the proposed SG-FCNN, the grid clipping strategy can only generate 327 sample patches, which is not enough for the SG-FCNN training. Hence, an overlapping clipping strategy was applied; each clipped patch shared a 75% overlapping area with the horizontally and vertically adjacent patches. In total, 5139 sample patches were generated in the training regions. To further improve the generalization ability of
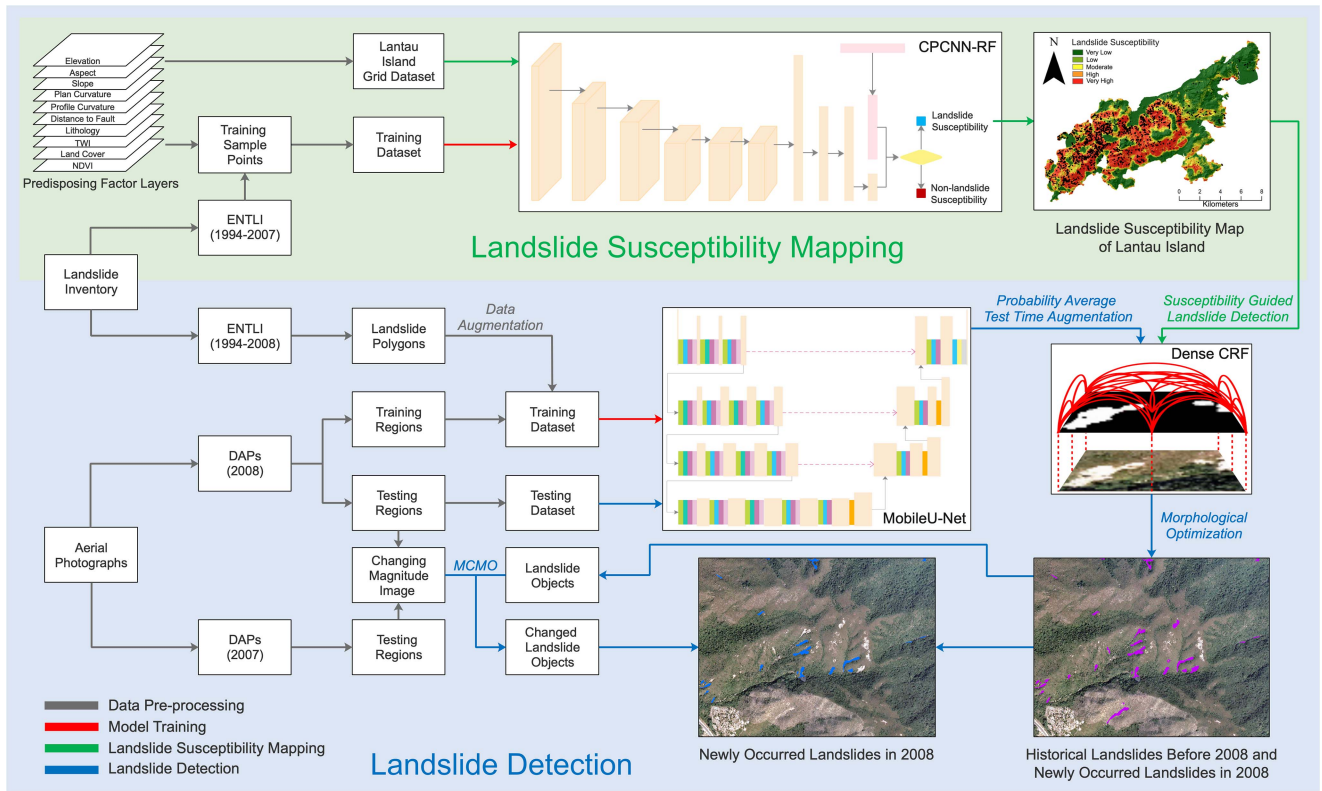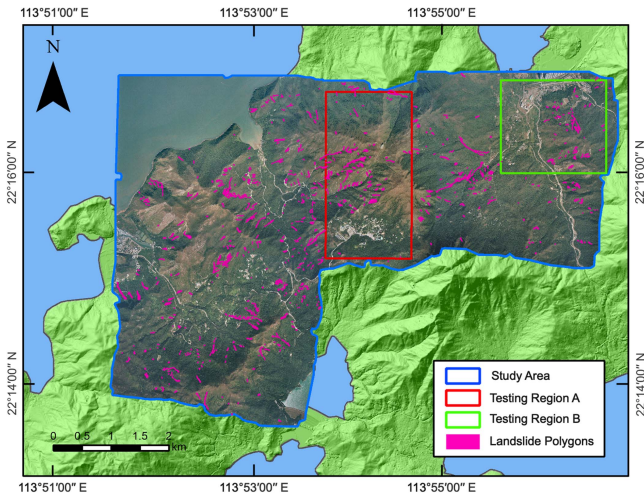
Fig. 3. Flowchart of the proposed SG-FCNN.

Fig. 4. Scope of study area and testing regions.

the SG-FCNN, data augmentation algorithms including flipping (horizontal/vertical), rotation (90°/180°/270°), averaging blur, Gaussian blur, bilateral blur, and adding random noise were adopted. Since landslides covered less than 10% of the training regions, data augmentation was only applied to square sample patches with landslide labels to balance the number of positive and negative pixels. In the end, 30 683 sample patches were generated and were further divided into training samples and validation samples at a proportion of 4:1.

B. Landslide Detection Using FCNN

1) MobileU-Net: The convolutional encoder–decoder architecture is utilized in most of the existing FCNN models. The high-level feature map of the input image is extracted in the encoder part using convolutional feature extractors, and the label of each pixel in the input image is predicted in the decoder part. U-Net [60] is one of the most successful convolutional encoder–decoder architectures, and has been applied in various tasks, including landslide detection. Compared to the traditional encoder–decoder architecture, U-Net applies the skip connection technique, which involves feature maps with different abstract levels in the decoder process. The skip connection effectively boosts semantic segmentation performance and substantially reduces the feature loss of the convolution operation in deep layers. The performance of the convolutional encoder–decoder-based models partly depends on the encoder structure. But the encoder of the original U-Net is the VGG-16, which is heavy and inefficient.

Inspired by the characteristics of U-Net, we modified the original U-Net and proposed the MobileU-Net (Fig. 5) to achieve the balance between performance and efficiency in the landslide detection task. The lightweight MobileNet-V2 [61] was applied as the backbone encoder for feature map extraction in the U-Net. Compared to the VGG-16 applied by the original U-Net, the MobileNet-V2 introduced a depthwise separable convolution block for feature map extraction, which can effectively save computation resources. The depthwise separable convolution
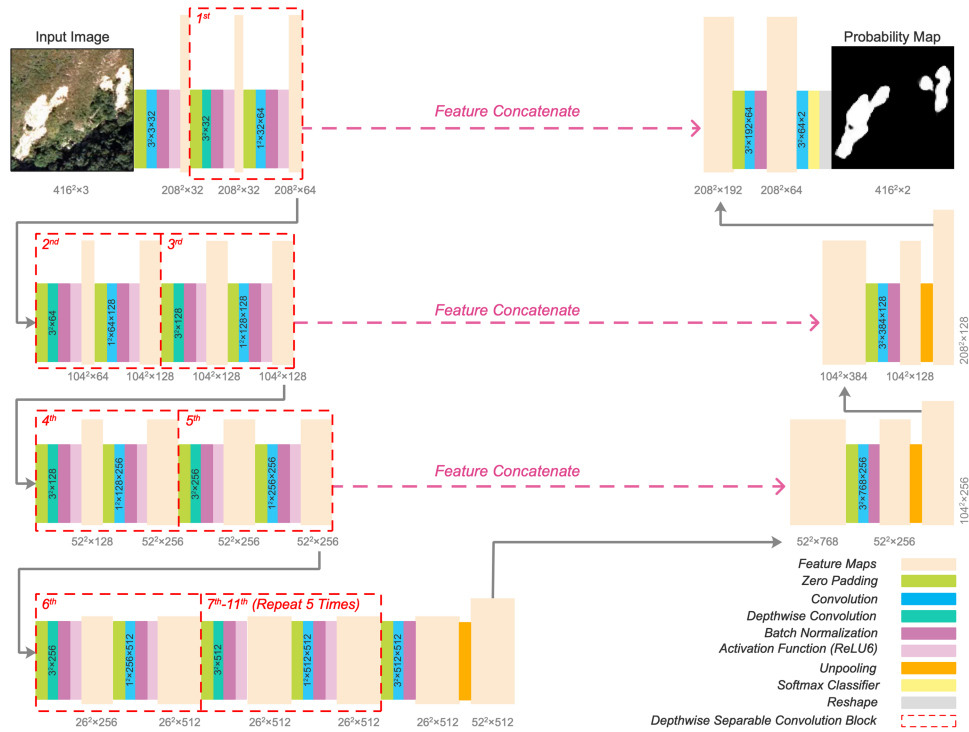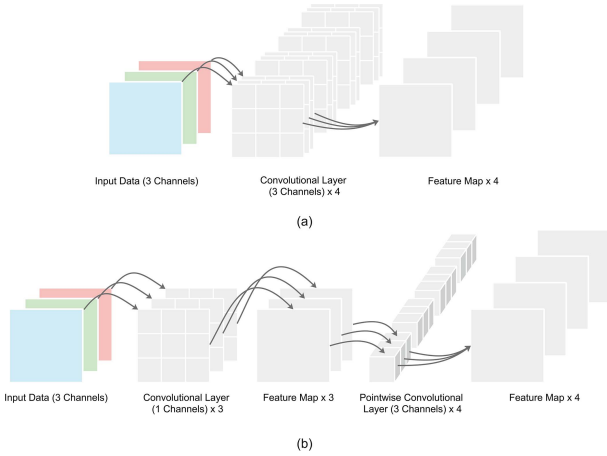
Fig. 5. Structure of mobile U-Net.

Fig. 6. Schematic of traditional convolution and depthwise convolution. (a) Traditional convolution. (b) Depthwise convolution.

block was composed of a depthwise convolution and a 1×1 original convolution (also called pointwise convolution). As shown in Fig. 6, by applying a single filter to each input channel, the depthwise convolution can extract high-level features in the spatial dimension and depth dimension. The subsequent pointwise convolution created a linear combination of depthwise convolution extracted features.

In the encoder part of MobileU-Net, a 3×3 original convolution and a total of 11 depthwise separable convolution blocks (with 3×3 deepwise convolution) were used for hierarchal high-level feature extraction. During the decoder process, feature maps extracted by the first, third, and fifth depthwise

separable convolution blocks were concatenated with the first, second, and third unsampled feature maps, respectively. In addition, considering that deconvolution operation has more trainable parameters compared with the combination of unpooling and traditional convolutional operation, the latter can also effectively avoid the checkerboard effect [62] and was applied for feature map upsampling. Finally, feature maps extracted by the last convolution layer in the decoder part were fed into the Softmax classifier to generate the pixelwise probability map of landslide detection.

Considering that the augmented dataset produced in Section III-A-2 was still too small to train MobileU-Net from scratch fully, a fine-tuning strategy was applied. The convolution parameters of MobileNet-V2 pretrained by the ImageNet image classification dataset were reloaded before the network training. Moreover, applying data augmentation to square sample patches with landslide labels enlarged the proportion of positive pixels, the percentage of negative pixels remained high. It may have led to MobileU-Net becoming more likely to misclassify landslide pixels into non-landslide pixels.

The Dice loss [63] and the weighted binary cross-entropy (BCE) loss [64] can both effectively avoid negative impacts caused by imbalanced samples in the training process. Significantly, the Dice loss can optimize the F_1-score of detected landslides directly. Thus, the compound loss function of the Dice loss and the weighted BCE loss was applied during the training process of the MobileU-Net, which is defined as follows:

$$\text{Compound Loss} = \text{Weighted BCE Loss} + \text{Dice Loss}$$
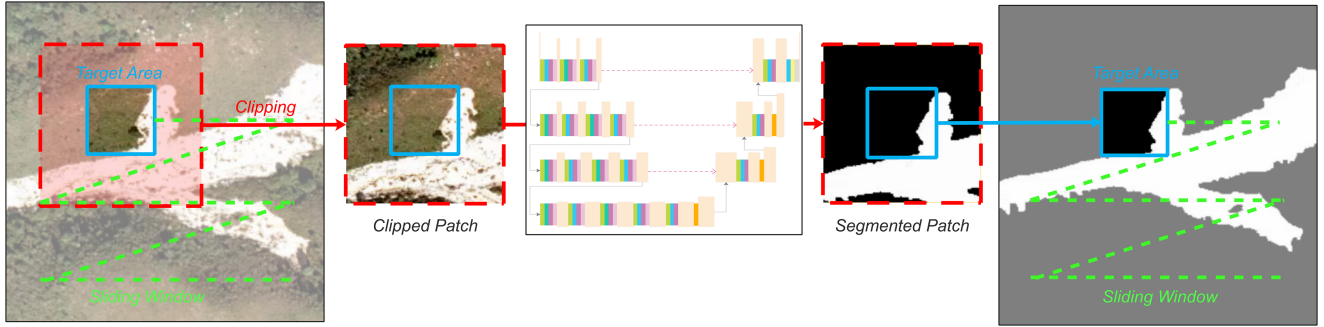$$= -[w(1 - y_{i,j}) \log(t_{i,j})$$

Fig. 7. Schematic of overlapping mosaic strategy.

$$+ (1 - w)\, y_{i,j} \log t_{i,j}] + 1$$
$$- \frac{2 \sum t_{i,j} y_{i,j} + \epsilon}{\sum t_{i,j} + \sum y_{i,j} + \epsilon} \tag{1}$$

for the pixel on the ith row and the jth column of each sample, and $y_{i,j}$ and $t_{i,j}$ represent the predicted label and the ground truth label, respectively. w stands for the ratio of landslide pixels to the total in the training dataset. ϵ is a constant with a Keras default value of 10^{-7}.

2) Overlapping Mosaic Detection Strategy: After the training process, MobileU-Net is prepared for landslide detection. Limited by the network structure, the input data size should have been restricted to $416 \times 416 \times 3$. Therefore, images of the testing regions cannot be fed into the MobileU-Net directly. Applying a grid-clipping strategy was a viable solution. However, the reliability of the landslide detection result near the boundary of the clipped patch was relatively poor. The problem was severe for some landslides that were clipped and divided into multiple patches. An overlapping detection mosaic strategy was applied (as shown in Fig. 7) to solve the above issues.

First, images of testing regions were clipped into several overlapped square image patches with a size of $416 \times 416 \times 3$, which was the same as the overlapping clipping strategy applied in the training dataset generation. Then, the clipped patches were fed into the MobileU-Net for pixelwise landslide detection. Next, the central region of the predicted patch was designated as the target area and clipped. Finally, a sliding-window strategy was applied to mosaic the detection result of predicted patches into seamless detection results. By utilizing the overlapping mosaic detection strategy, only the highly reliable central region of the predicted patch was retained.

C. Landslide Detection Using SG-FCNN

To further boost the detection performance of the FCNN, this section innovatively proposed the SG-FCNN by applying the probability average test time augmentation PA-TTA and the SG strategy. The MCMO change detection strategy is also proposed to detect newly occurred landslides using SG-FCNN.

1) Probability Average Test Time Augmentation (PA-TTA): To reduce the miss detection rate of the FCNN, the PA-TTA was first proposed. The overlapping clipped image patches in the testing region were augmented using the same augmentation

methods applied to the training data. For each augmentation method, a probability map of landslide detection was obtained using FCNN and the overlapping mosaic detection strategy. Then, all probability maps based on different augmentation methods were averaged

$$\text{AP}\ (P_c) = \frac{\sum_i \text{PP}_i}{i} \tag{2}$$

where P_c stands for the cth pixel in testing region. PP_i is the prediction probability of the ith augmentation method. $\text{AP}(P_c)$ denotes the averaged prediction probability of P_c. If $\text{AP}(P_c)$ exceeds 20%, the pixel P_c would be kept as landslide candidates, while others were considered fuzzy boundaries and were discarded. Finally, the generated candidate pixels were converted into landslide candidate objects based on the eight-neighborhood pixel-object conversion criteria [51], [65].

2) Landslide Detection Under the Guidance of Susceptibility: Even though the proposed FCNN has applied advanced DL techniques, false detection of other land cover features, such as muddy roads and buildings that could be misclassified as landslides, remained inevitable. Hence, additional postprocessing is necessary to remove falsely detected landslides.

Landslide susceptibility maps can portray the spatial probability of landslide occurrence in the near future [54], [55], which is obtained based on the analysis of landslide-related auxiliary information (also known as landslide predisposing factors) [66]. Landslide susceptibility mapping methods have been reviewed comprehensively by some scholars [5], [54], [67] and thus are not covered in this article. Recent articles have shown that methods based on CNN also perform the best in landslide susceptibility mapping [31], [68], [69], [70]. If the CNN-predicted landslide susceptibility can be used as prior knowledge in the detection process, it is promising to further improve the detection perforce of FCNN.

Thus, the CNN-predicted landslide susceptibility was introduced as prior knowledge to remove falsely detected landslides as follows:

$$\text{SLDP}\ (O_a) = \frac{\sum [\text{LS}\,(P_b) \times \text{LDP}\,(P_b)]}{N}\ ,\ P_b \in O_a. \tag{3}$$

For the ath landslide candidate object O_a, the P_b and N stand for the bth pixel and the total number of pixels in O_a, respectively. For pixel P_b, $\text{LDP}(P_b)$ represents the landslide detection probability of P_b and $\text{LS}(P_b)$ denotes the probability

value of CNN-predicted landslide susceptibility. $\text{SLDP}(O_a)$ represents the SG landslide detection probability of O_a, and is obtained by averaging $\text{LS}(P_b) \times \text{LDP}(P_b)$. The threshold of susceptibility guidance, T_{SLDP}, was set as 20% based on the division of five equal intervals, which indicated a very low SG landslide detection probability. If $\text{SLDP}(O_a)$ is lower than T_{SLDP}, the landslide candidate object O_a would be identified as a falsely detected landslide and removed. If $\text{SLDP}(O_a)$ is higher than T_{SLDP}, the landslide candidate object O_a would be identified as a correctly detected landslide and retained.

3) Boundary and Morphological Optimization: In the SG-FCNN, boundary and morphological optimization (BMO) was applied to enhance the precision of detected landslides further. In the MobileU-Net, feature maps extracted by the encoder had lower resolution than the input image. To obtain pixelwise landslide detection results of the same size as the input image, an unpooling and convolution operation was applied to low-resolution feature maps in the decoder part. However, the input image was not involved in the decoder part; thus, the detected landslides' boundary is coarse and fails to fit the actual boundary.

The Dense CRF [71] was applied based on aerial images' spectral and textural features to refine the boundary of detected landslides. Compared to the traditional CRF, which only utilizes the connections between the target pixel and its adjacent pixels, the Dense CRF can utilize the connections between all pixel pairs of the input image and refine the boundary of the detected landslides in greater detail. The Dense CRF confirmed to Gibbs distribution

$$P\ (x\ =\ X|I) = \frac{\exp\left(-E\left(X|I\right)\right)}{Z\left(I\right)} \qquad (4)$$

where I is the input image and x is the predicted result to be optimized. $E(X|I)$ is the Gibbs energy, which is composed of unary potential $\psi_u(x_i)$ and pairwise potential $\psi_p(x_i, y_j)$ as a following formula:

$$E\ (x|I) = \sum_i \psi_u\left(x_i\right) + \sum_{i,j} \psi_p\left(x_i, y_j\right) \qquad (5)$$

$$\psi_u\left(x_i\right) = -\log P\left(x_i\right) \qquad (6)$$

$$\psi_p\left(x_i, y_j\right) = \mu\left(x_i, y_j\right)$$

$$\times \left[\underbrace{w^1 \exp\left(-\frac{|p_i - p_j|^2}{2\theta_\alpha^2} - \frac{|I_i - I_j|^2}{2\theta_\beta^2}\right)}_{\text{Appearance Kernel}} + \underbrace{w^2 \exp\left(-\frac{|p_i - p_j|^2}{2\theta_\gamma^2}\right)}_{\text{Smoothness Kernel}} \right]$$
$$(7)$$

where $\mu(x_i, y_j)$ is the label compatibility. w^1 and w^2 are the weights of appearance kernel potential and smoothness kernel potential, respectively. The appearance kernel potential is used for clustering pixels with similar spectral features into the same class, in which θ_a and θ_b are the degree of spatial nearness and spectral similarity. The smoothness kernel potential is applied to remove isolated regions [72] with a spatial nearness degree controlled by θ_γ.

After the Dense CRF optimized the boundaries of the detected landslides, two widely used morphological optimization algorithms, namely, area opening and hole filling [73], [74], were implemented to improve the detection accuracy further. The area opening was applied to remove those detected landslides that were unreasonably small, while the hole filling was applied to fill up those small holes inside correctly detected landslides.

4) Detection of Newly Occurred Landslides Based on MCMO: Landslides detected by the SG-FCNN have the advantages of high accuracy and reliability, making them suitable as the basis for detecting newly occurred landslides. As reviewed in Section I, the FCNN has also achieved state-of-the-art performance in detecting newly occurred landslides. However, the unsupervised CMI-based change detection strategies have unique advantages in efficiency [75] and are still widely applied in practical applications. Thus, combining the proposed SG-FCNN with the CMI-based change detection strategy is a promising way to improve the detection performance of newly occurred landslides.

Based on the proposed SG-FCNN, this article further proposed an unsupervised change detection strategy, MCMO, to detect newly occurred landslides based on bitemporal images and the landslide detection results from postlandslide images. First, the CMI is generated based on the coregistered postlandslide and prelandslide images

$$\text{CM}\ (P_c) = \frac{\sum_i abs\left(DN_i^{\text{Pre}} - DN_i^{\text{Post}}\right)}{255 \times N_i} \qquad (8)$$

where P_c stands for the cth pixel in testing region. DN_i^{Pre} and DN_i^{Post} are the grey value of P_c in the ith band of the prelandslide image and postlandslide image, respectively. The greater the $\text{CM}(P_c)$, the greater the change has been experienced. Then, based on the changing magnitude of each pixel, the historical landslides can be removed from the landslide detection results of postlandslide images as follows:

$$\text{MCM}\ (O_e) = \frac{\sum \left[\text{CM}\left(P_d\right)\right]}{N}\ ,\ P_d \in O_e \qquad (9)$$

where O_e stands for the eth detected landslide objects of the postlandslide image. For O_e, $\text{CM}(P_d)$ is the changing magnitude of the dth pixel, and N is the total number of pixels. Therefore, $\text{MCM}(O_e)$ denotes the mean changing magnitude of O_e. T_{MCM} is the threshold for judging whether O_e has changed or not. If $\text{MCM}(O_e)$ exceeds T_{MCM}, the detected landslide object O_e would be identified as a historical landslide or other unchanged land cover features. T_{MCM} was set to 25% based on trial and error. Finally, the proposed MCMO strategy obtained the detection result of newly occurred landslides by deleting those O_e with an MCM value above T_{MCM}.

IV. Experiments and Results

The landslide susceptibility mapping and landslide detection experiments were carried out on a Windows 10 OS with a 3.6 GHz Core i7-7700 and an NVIDIA GeForce GTX 1080. TensorFlow-GPU 1.7.0 was selected as the DL platform for implementing the FCNN, the SG-FCNN, and the CPCNN-RF.
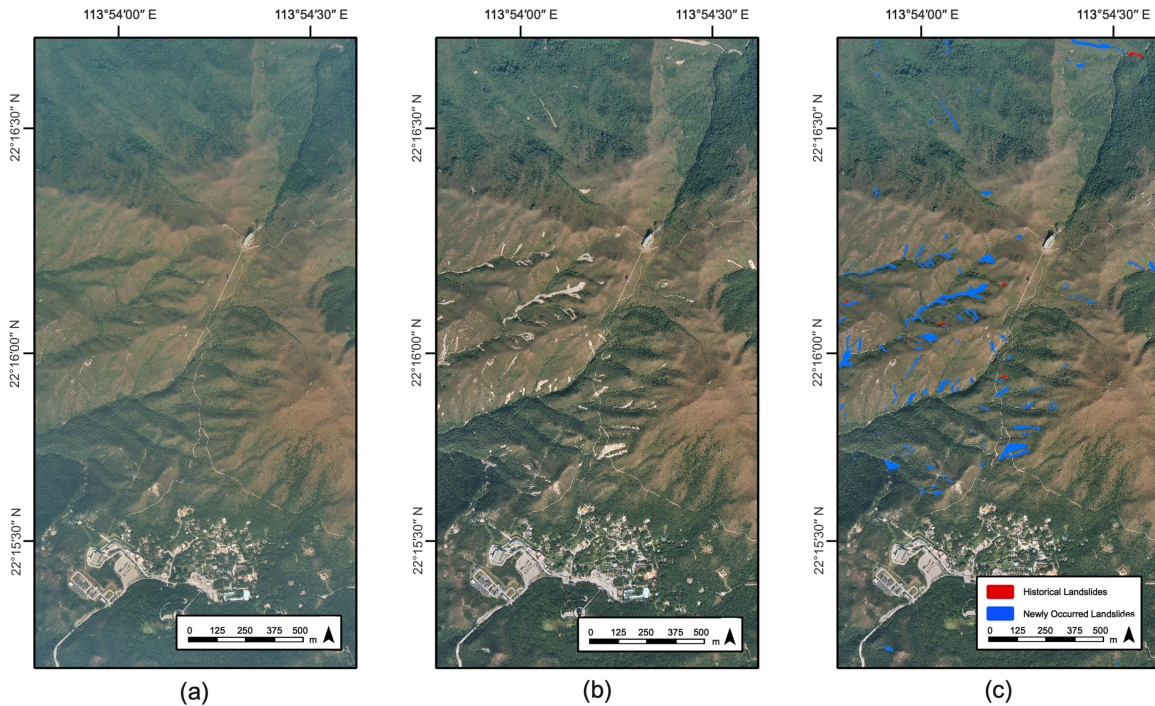
Fig. 8.   DAPs and evaluation samples in testing region A. (a) DAP 2007. (b) DAP 2008. (c) Evaluation samples overlaid on DAP 2008.
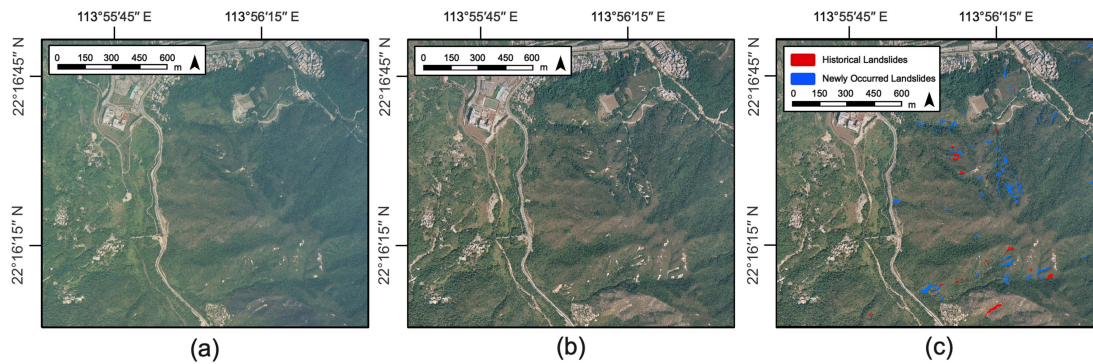

Fig. 9.   DAPs and evaluation samples in testing region B. (a) DAP 2007. (b) DAP 2008. (c) Evaluation samples overlaid on DAP 2008.

TABLE I
STATISTICAL DETAILS OF EVALUATION SAMPLES

	Total area (m^2)	All landslides		Newly occurred landslides		Historical landslides	
		Number	Area (m^2)	Number	Area (m^2)	Number	Area (m^2)
Testing region A	4 292 166	106	60 621	100	59 129	6	1492
Testing region B	2 936 253	70	21 785	54	17 284	16	4501
Total	7 228 419	176	82 406	154	76 413	22	5993

The Dense CRF model was implemented with Python wrapper, pydensecrf 1.0rc3 (https://github.com/lucasb-eyer/pydensecrf).

There were two missions in this article: detecting all landslides (including historical and newly occurred landslides) in 2008 and detecting newly occurred landslides in 2008. To evaluate the detection performance in two testing regions, two ground truth datasets were visually delineated by reference to the ENTLI (from 1994 to 2008) and coregistered DAPs (2007 and 2008), as shown in Figs. 8 and 9. The statistical details of the evaluation samples are given in Table I.

A. Detection of All Landslides

During the training procedure of the FCNN, an Adam optimization algorithm was selected to update the networks' weights iteratively. Considering the hardware performance of the

experimental environment, the batch size and the initial learning rate were set as 8 and 0.001, respectively. If the validation loss did not decrease within three epochs, the learning rate would reduce by 90%. The early stopping strategy was applied based on validation loss to avoid overfitting. The network training would be terminated if the validation loss did not decrease within 10 epochs.

As for the overlapping mosaic detection strategy, the target area constituted 5% of the corresponding predicted patch. The hyperparameters of the Dense CRF, namely, θ_a, θ_β, θ_γ, w^1, and w^2, were set to 30, 20, 1.0, 1.5, and 1.0 in testing region A, and were set to 30, 10, 1.0, 1.1, and 1.0 in testing region B, according to the suggestion of Kra¨henbu¨hl and Koltun [71] and the optimization experience of Shi in Lantau Island [51]. The Dense CRF optimized the initial detection results for 10 iterations. Taking the characteristics of landslides and ground dataset on Lantau Island into account, the thresholds for area opening and hole filling were set as 25 and 200 m^2, respectively.

When detecting landslides using the SG-FCNN, we applied the landslide susceptibility map generated by the state-of-the-art CPCNN-RF. All details of the CPCNN-RF and susceptibility mapping process in Lantau Island can be found in [31]. It cannot present all details about the CPCNN-RF due to space limitations.

The CPCNN-RF was trained based on 10 landslide predisposing factor layers of Lantau Island and landslide crowns recorded in the ENTLI (from 1994 to 2007). The applied landslide predisposing factor layers had a spatial resolution of 30 m, which included elevation, aspect, slope, plan curvature, profile curvature, distance to fault, lithology, topographic wetness index (TWI), land cover, and NDVI. Elevation, slope, aspect, profile curvature, and plan curvature were calculated using the digital elevation model (DEM) (30 m per pixel) provided by Esri China (HK). Lithological and fault lines were extracted from the simplified geological map provided by Esri China (HK). TWI was calculated from DEM using hydrology tools in ArcGIS. Land cover was obtained from the FROM-GLC product (30 m per pixel) [76]. NDVI was calculated using Landsat TM images with 30-m spatial resolution, which was taken on 14th March 2006. After training ended, the predisposing factor layers of Lantau Island were divided into 163 052 grids with a spatial resolution of 30 m and fed into the trained CPCNN-RF for landslide susceptibility mapping. The derived landslide susceptibility map is given in Fig. 10, which has been ranked into five grades.

Landslide crowns recorded in the ENTLI (from 1994 to 2007) were used as testing samples to evaluate the reliability of the derived landslide susceptibility map. The OA and the area under the receiver operating characteristic curve were determined in SPSS Statistic 26 as statistical evaluation metrics. The evaluation results illustrated that the landslide susceptibility map generated by the CPCNN-RF has achieved satisfactory accuracy, which qualified it to be used as an indicator to distinguish the areas that were not prone to landslide occurrence.

For the two testing regions, Figs. 11 and 12 show the intermediate process of the SG-FCNN. Figs. 13 and 14 show the detection results of all landslides in 2008.
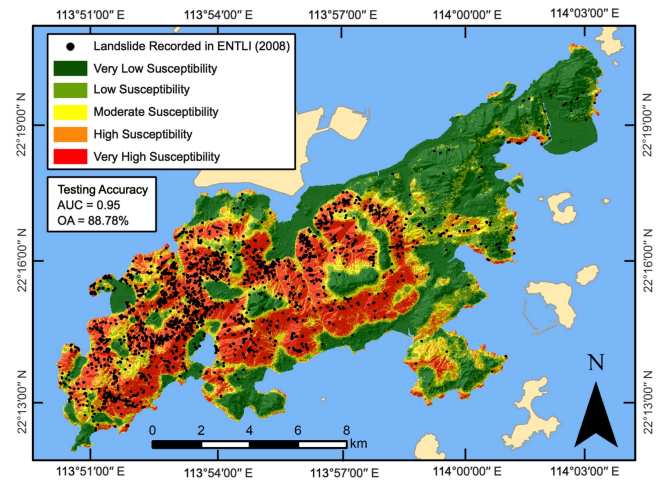

Fig. 10. Landslide susceptibility map generated by CPCNN-RF based on ENTLI (1994–2007) [31].

To highlight the superiority of the proposed SG-FCNN, we further compared it with the PBCNN, the FCNN, and the FCNN with postprocessing based on auxiliary information. The applied PBCNN is the per superpixel multiscale CNN based on SEEDS (SEEDS–MCNN) [26] with a MobileNet-V2 backbone. The applied FCNN includes the original U-Net (with VGG-16 backbone) [60], DeepLab-V3 (with MobileNet-V2 backbone) [61], and the proposed MobileU-Net. The postprocessing strategy based on auxiliary information is referenced to Shi's strategy for FCNN-based landslide detection in Lantau Island [51]: Creating a buffer zone based on road vectors with a distance of 10 m. If the overlapping area of the landslide object and buffer zone exceeds 30% of the landslide object, discard the corresponding landslide object. If more than 50% area of the landslide object with a slope less than 10°, discard the corresponding landslide object. The applied road vector of Lantau Island was downloaded from https://www.openstreetmap.org. The slope map of Lantau Island was calculated based on the DEM with a spatial resolution of 5 m, provided by ESRI Hong Kong. All comparative models mentioned above were pretrained by the ImageNet image classification dataset and applied the training data augmentation strategy mentioned in Section III-A-2. All FCNN-based comparative models applied the overlapping mosaic detection strategy mentioned in Section III-B-1.

B. Detection of Newly Occurred Landslides

Landslides detected by the SG-FCNN in the DAPs (2008) were used as the basis for detecting newly occurred landslides in 2008. The CMI of the two testing areas was generated based on the coregistered DAPs (2007) and DAPs (2008), using ArcMap 10.3. Figs. 15 and 16 illustrate the intermediate process of the SG-FCNN with MCMO strategy in testing region A and B. Figs. 17 and 18 represent the detection results of newly occurred landslides in 2008.

The proposed MCMO change detection strategy was compared with the change detection strategy applied by the
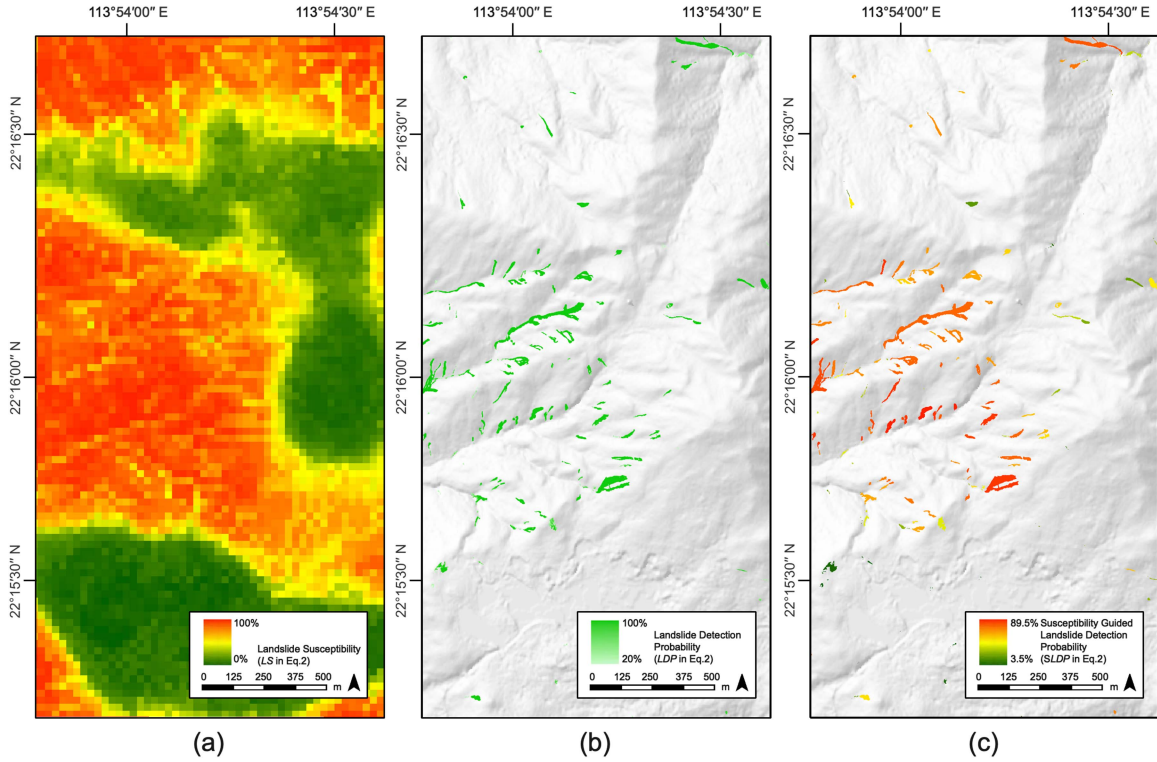
Fig. 11. Intermediate process of SG-FCNN in testing region A. (a) Landslide susceptibility. (b) Landslide detection probability. (c) Susceptibility-guided landslide detection probability.
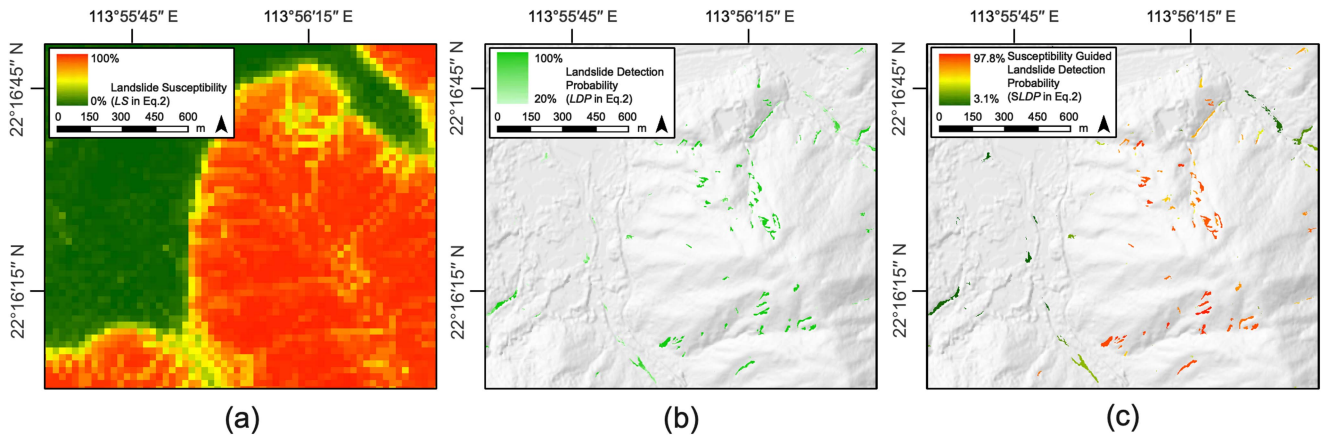

Fig. 12. Intermediate process of SG-FCNN in testing region B. (a) Landslide susceptibility. (b) Landslide detection probability. (c) Susceptibility-guided landslide detection probability.

object-oriented change detection CNN (CDCNN) [51]. In the CDCNN, FCNN is used to detect landslides from prelandslide and postlandslide images separately. Based on this, newly occurred landslides are identified by analyzing the IoU of paired landslide objects detected from the prelandslide and postlandslide images. If a landslide object detected in the postlandslide image failed to pair with a landslide object in the prelandslide image, or the IoU of paired landslide objects is less than 50%, the corresponding landslide is newly occurred.

C. Evaluation of Detection Results

Four widely used metrics, including precision, recall, F_1 score, and IoU were applied and can be defined by the following equations:

$$\text{Precision} = \frac{\text{PN}_a}{\text{PN}_b} \tag{10}$$

$$\text{Recall} = \frac{\text{PN}_a}{\text{PN}_c} \tag{11}$$

Fig. 13. Detection results of all landslides in testing region A. (a) Ground truth. (b) PBCNN (SEEDS–MCNN) [26]. (c) FCNN (original U-Net) [60]. (d) FCNN (DeepLab-V3) [61]. (e) FCNN (MobileU-Net). (f) FCNN (MobileU-Net) + PA-TTA. (g) FCNN (MobileU-Net) + BMO. (h) FCNN (MobileU-Net) + BMO + post-processing strategy based on auxiliary information [51]. (i) SG-FCNN (MobileU-Net) + BMO.
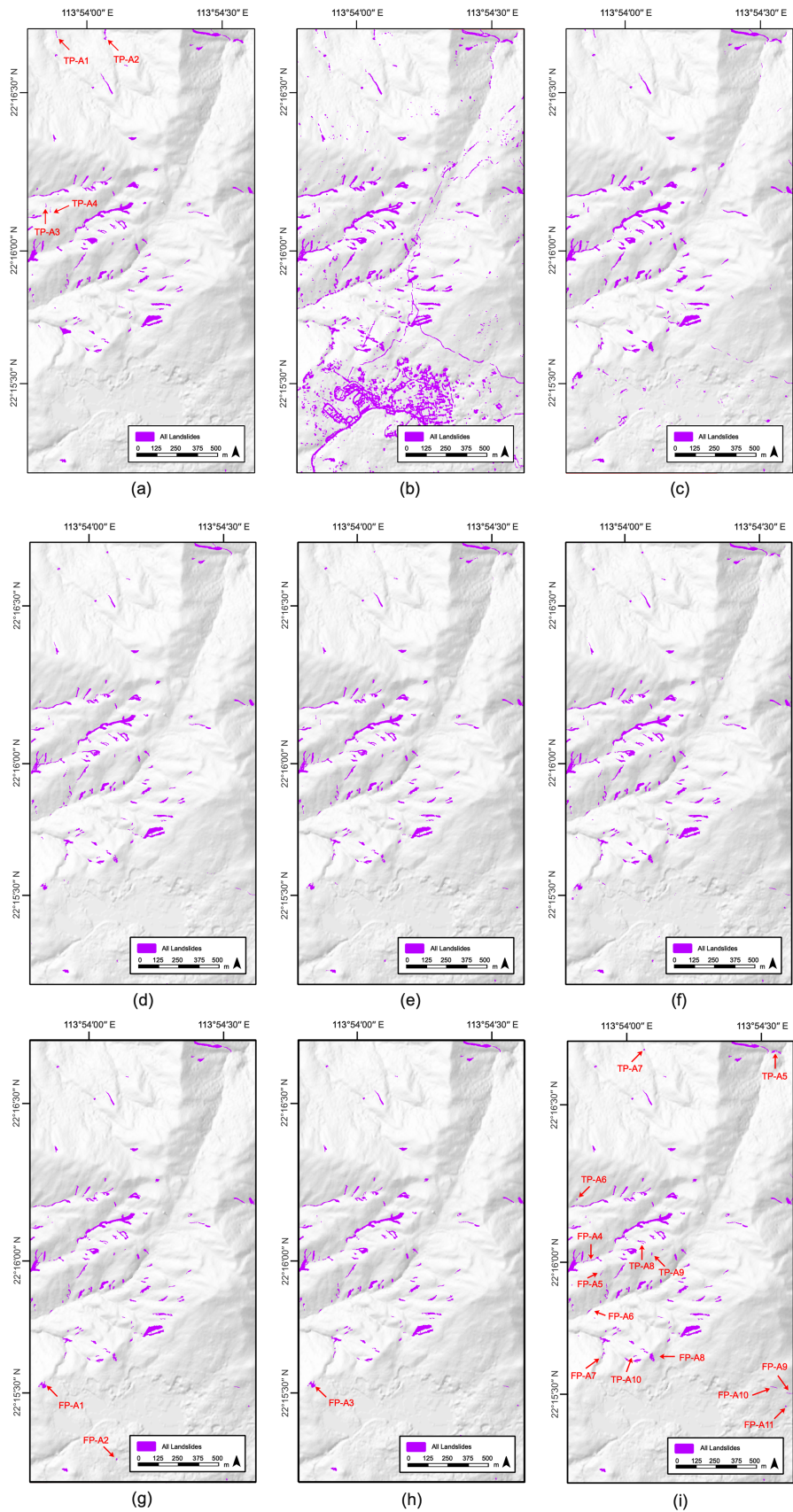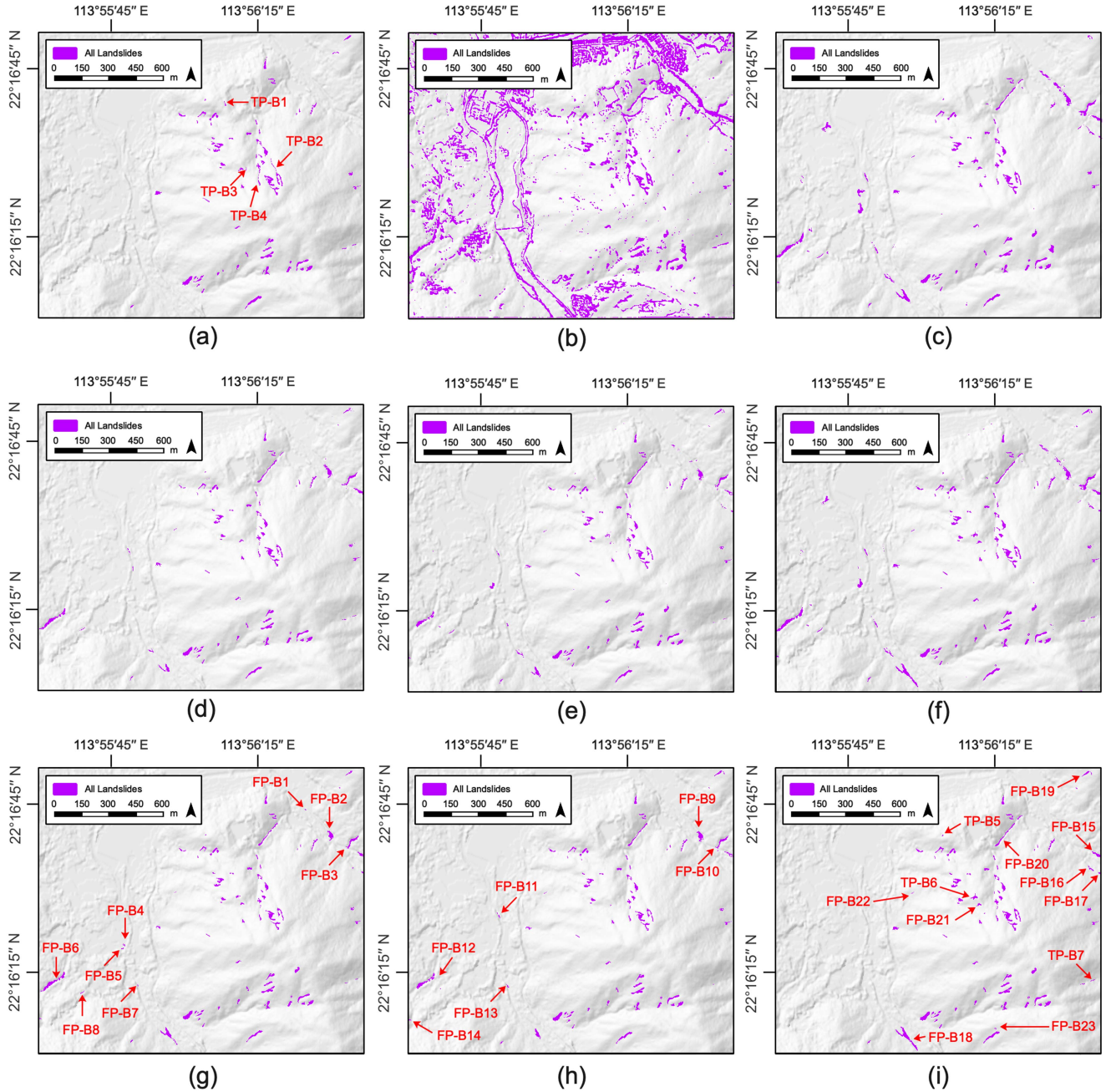
Fig. 14. Detection results of all landslides in testing region B. (a) Ground truth. (b) PBCNN (SEEDS-MCNN) [26]. (c) FCNN (original U-Net) [60]. (d) FCNN (DeepLab-V3) [61]. (e) FCNN (MobileU-Net). (f) FCNN (MobileU-Net) + PA-TTA. (g) FCNN (MobileU-Net) + BMO. (h) FCNN (MobileU-Net) + BMO + postprocessing strategy based on auxiliary information [51]. (i) SG-FCNN (MobileU-Net) + BMO.

$$F_1\text{Score} = \frac{2 \times \text{Precision} \times \text{Recall}}{\text{Precision} + \text{Recall}} \qquad (12)$$

$$\text{IoU} = \frac{\text{PN}_a}{\text{PN}_c + \text{PN}_d} \qquad (13)$$

where PN_a stands for the pixel number of correctly detected landslides. PN_b is the pixel number of detected landslides. PN_c is stands for the pixel number of landslide ground truth. PN_d is the pixel number of detected landslide that is not matched with corresponding ground truth. Precision measures the proportion

of correctly predicted landslide pixels in predicted landslide pixels. Recall measures the proportion of landslide pixels that are correctly detected. F_1 Score and IoU are both comprehensive indexes. The F_1 Score is the harmonic mean of precision and recall, and the IoU measures the extent of the overlap of detected landslides and ground truth. The evaluation results of the two testing regions are given in Tables II and III.

While detecting all landslides in 2008, the FCNN was superior to the PBCNN. The detection accuracy of the MobileU-Net was much higher than that of the original U-Net and is comparable to that of the MobileU-Net. The MobileU-Net only have 6
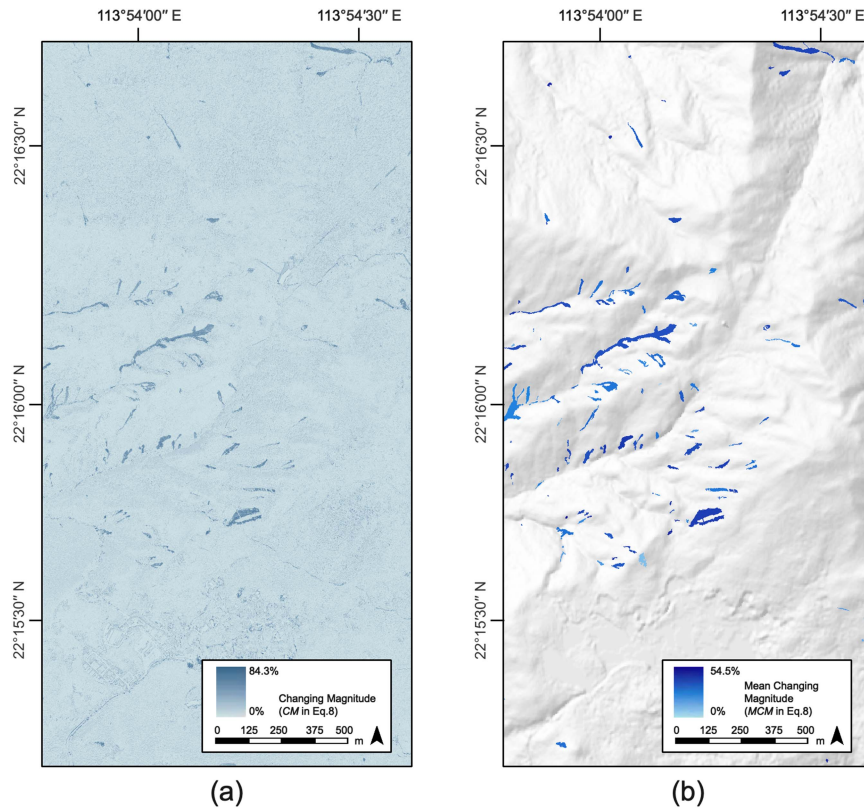
Fig. 15. Intermediate process of the SG-FCNN with MCMO in testing region A. (a) Changing magnitude. (b) Mean changing magnitude.
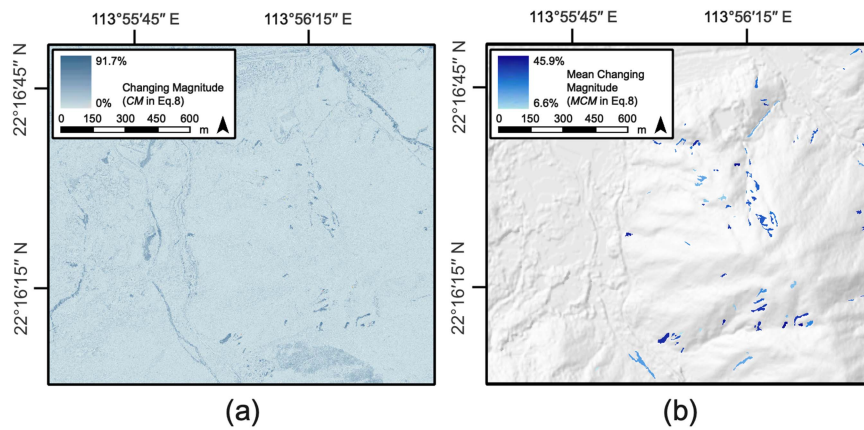

Fig. 16. Intermediate process of the SG-FCNN with MCMO in testing region B. (a) Changing magnitude. (b) Mean changing magnitude.

315 522 parameters, which is only half of that of the original U-Net and one-third of that of the DeepLab-V3. Thus, the MobileU-Net is much more efficient and has the best comprehensive performance among all FCNN models. With the help of the susceptibility guidance strategy, the detection accuracy of the proposed SG-FCNN was improved significantly compared to the original FCNN. In particular, the SG-FCNN with BMO achieved the outstanding performance with the highest precision, F_1 Score, and IoU in all testing regions. However, a small number of land cover features were falsely identified as landslides by the SG-FCNN.

While detecting newly occurred landslides in 2008, the detection accuracy of the SG-FCNN with the proposed MCMO change detection strategy was significantly improved compared with the SG-FCNN with the change detection strategy of CD-CNN [51]. In addition, no matter what change detection strategy was combined with the proposed SG-FCNN, the detection accuracy of newly occurred landslides was higher than the detection accuracy of all landslides. Especially in testing region B, by utilizing the proposed MCMO change detection strategy, the detection accuracy of newly occurred landslides was sharply improved compared with the detection accuracy of all landslides.
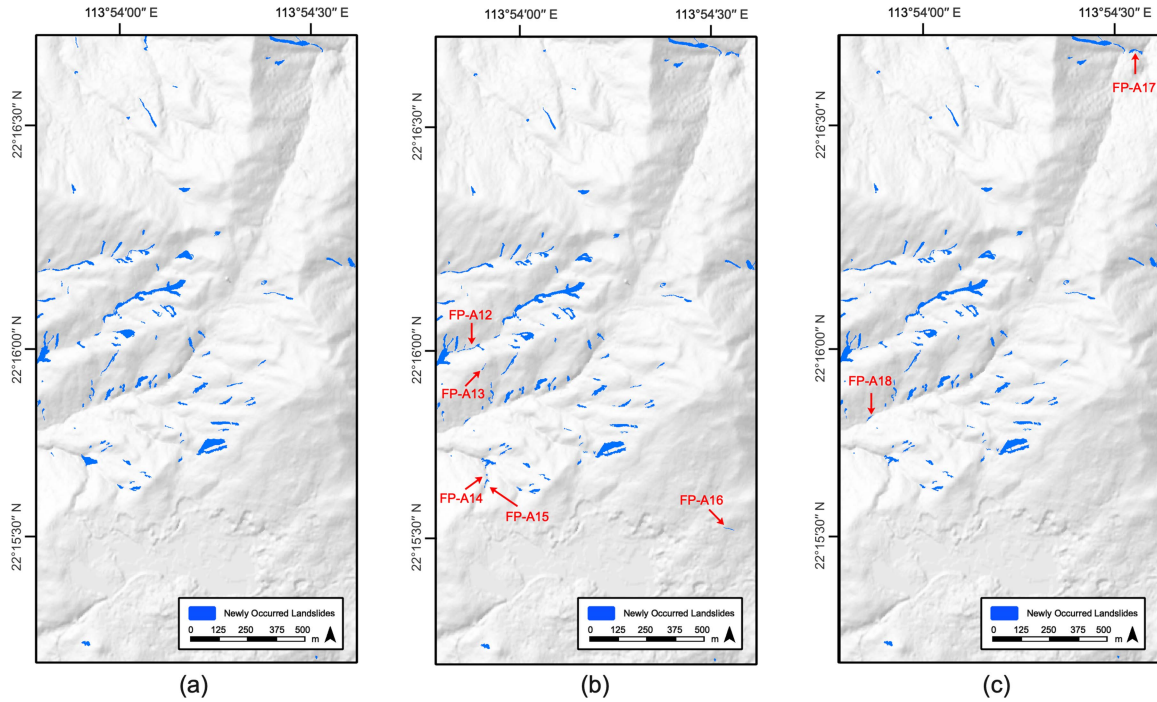
Fig. 17. Detection results of newly occurred landslides in testing region A. (a) Ground truth of newly occurred landslides in 2008. (b) SG-FCNN + change detection strategy of CDCNN [51]. (c) SG-FCNN + MCMO change detection strategy.
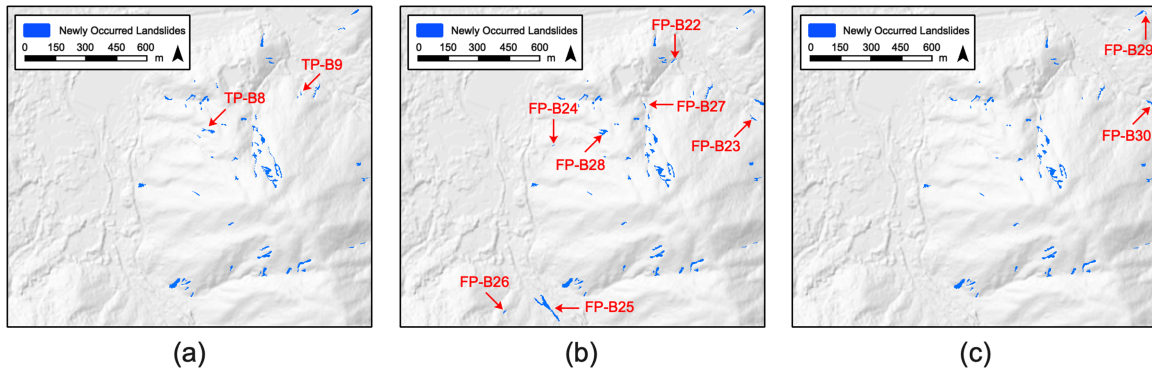

Fig. 18. Detection results of newly occurred landslides in testing region B. (a) Ground truth of newly occurred landslides in 2008. (b) SG-FCNN + change detection strategy of CDCNN [51]. (c) SG-FCNN + MCMO change detection strategy.

V. DISCUSSION

A. Effectiveness of Susceptibility Guidance Strategy

This article modified the FCNN and innovatively proposed the SG-FCNN by introducing the susceptibility guidance strategy. For each landslide candidate object, its averaged probability of landslide detection merged with the landslide susceptible probability.

In the proposed SG-FCNN, visual and environmental conditions would be considered simultaneously during the detection process. Landslide candidates with low visual detection probability in high landslide susceptibility zones can be detected [see TP-A5 and TP-A6 in Fig. 13(i)]. In contrast, landslide candidates with high detection visual probability in low landslide susceptibility zones can be discarded [see FP-A1 and FP-A2 in Fig. 13(g), FP-B1 to FP-B8 in Fig. 14(g)]. Tables II and III show that the SG-FCNN is superior to the original MobileU-Net and the MobileU-Net with PA-TTA on all evaluation indices. In testing region A, the F_1 Score and IoU of the SG-FCNN reached 0.9049 and 82.63%, respectively. In testing region B, the SG-FCNN achieved an F_1 Score of 0.7938 and an IoU of 65.81%.

Compared to the state-of-the-art postprocessing method based on auxiliary information (road vectors, building vectors, and slope) [51], the proposed SG-FCNN also has a clear lead on all evaluation indices. Compared to the SG-FCNN, FP-A3 in Fig. 13(h) and FP-B9 to FP-B14 in Fig. 14(h) were falsely detected, TP-A5 to TP-A10 in Fig. 13(i) and TP-B5 to TP-B7 in Fig. 14(i) were not detected. The reason for the success of the proposed SG-FCNN is that it extracted knowledge (landslide

TABLE II
QUANTITATIVE EVALUATION RESULTS OF LANDSLIDE DETECTION RESULTS IN TESTING REGION A

Detection mission	Method	Implementation details	Precision (%)	Recall (%)	F_1 Score	IoU (%)
All landslides (historical and newly occurred)	PBCNN	SEEDS–MCNN (with MobileNet-V2 Backbone) [26]	19.45	93.61	0.3221	19.19
	FCNN	Original U-Net (with VGG-16 Backbone) [60]	60.89	90.46	0.7279	57.22
		Deeplab V3 (with MobileNet-V2 Backbone) [61]	85.05	87.25	0.8615	75.67
		MobileU-Net	85.44	89.39	0.8737	77.57
		MobileU-Net + MV-TTA	86.32	88.52	0.8741	77.63
		MobileU-Net + PA-TTA	79.38	**93.53**	0.8587	75.25
		MobileU-Net + BMO	91.43	84.79	0.8799	78.55
		MobileU-Net + Postprocessing strategy based on auxiliary information [51]	86.77	88.46	0.8761	77.95
		MobileU-Net + BMO + Postprocessing strategy based on auxiliary information [51]	**93.01**	85.03	**0.8884**	**79.93**
	SG-FCNN	SG-FCNN (MobileU-Net + PA-TTA + Susceptibility guidance strategy)	82.63	**93.52**	0.8774	78.16
		SG-FCNN + BMO	**91.17**	89.81	**0.9049**	**82.63**
Newly occurred landslides	SG-FCNN	SG-FCNN + BMO + Change detection strategy of CDCNN [51]	92.36	89.91	0.9112	83.69
		SG-FCNN + BMO + MCMO Change detection strategy	**93.54**	**89.91**	**0.9169**	**84.65**

TABLE III
QUANTITATIVE EVALUATION RESULTS OF LANDSLIDE DETECTION RESULTS IN TESTING REGION B

Detection mission	Method	Implementation details	Precision (%)	Recall (%)	F_1 score	IoU (%)
	PBCNN	SEEDS--MCNN (with MobileNet-V2 Backbone) [26]	5.36	94.70	0.1014	5.34
All landslides (historical and newly occurred)	FCNN	Original U-Net (with VGG-16 Backbone) [60]	46.37	80.48	0.5884	41.68
		Deeplab V3 (with MobileNet-V2 Backbone) [61]	67.31	79.94	0.7309	57.59
		MobileU-Net	64.72	79.20	0.7124	55.32
		MobileU-Net + MV-TTA	65.47	78.02	0.7120	55.28
		MobileU-Net + PA-TTA	53.14	**87.93**	0.6624	49.53
		MobileU-Net + BMO	67.23	75.53	0.7114	55.20
		MobileU-Net + Postprocessing strategy based on auxiliary information [51]	70.06	79.25	0.7437	59.20
		MobileU-Net + BMO + Postprocessing strategy based on auxiliary information [51]	**72.82**	76.72	**0.7472**	**59.64**
	SG-FCNN	SG-FCNN (MobileU-Net + PA-TTA + Susceptibility guidance strategy)	71.12	**87.93**	0.7864	64.80
		SG-FCNN + BMO	**73.89**	85.74	**0.7938**	**65.81**
Newly occurred landslides	SG-FCNN	SG-FCNN + BMO + Change detection strategy of CDCNN [51]	75.29	**85.98**	0.8029	67.07
		SG-FCNN + BMO + MCMO Change detection strategy	**89.57**	83.42	**0.8638**	**76.03**

susceptibility) from auxiliary information (landslide predisposing factors and the distribution of historical landsides) instead of using auxiliary information directly. As prior knowledge, landslide susceptibility condenses assorted auxiliary information related to landslide occurrence and considers the occurrence rule of historical landslides simultaneously. Given the above, introducing landslide susceptibility can significantly improve the detection accuracy of FCNN and expand the application range of landslide susceptibility.

B. Effectiveness and Indispensability of PA-TTA and Susceptibility Guidance

While aiming to improve the detection accuracy of the FCNN, this article proposed an SG-FCNN that used PA-TTA and innovatively introduced landslide susceptibility as prior knowledge for landslide detection. After the FCNN initially detected the landslides, the PA-TTA was applied, and landslide susceptibility was involved in guiding the detection process. Misdetections

were avoided, and false detections were eliminated, thus, adding to the accuracy of the landslide detection.

There are three reasons for applying the PA-TTA rather than the max voting test time augmentation (MV-TTA). First, the MV-TTA has few advantages in landslide detection. As shown in Tables II and III, the detection accuracy of the MobileU-Net slightly increased after applying the MV-TTA. Second, the PA-TTA is implemented based on the probability map instead of the binary detection result. Thus, a generated average probability map of landslide detection can be analyzed with a landslide susceptibility map, and SG landslide detection can be realized. Third, the proposed PA-TTA only discarded those pixels with very low averaged probability and can detect more landslide candidates than the original FCNN with or without the MV-TTA. As presented in Table II and III, applying the PA-TTA can effectively avoid the misdetection of landslides with a significantly higher recall.

Compared with applying the MV-TTA, applying the PA-TTA would result in lower precision and high recall rate because the probability threshold of the PA-TTA is set as 20% instead of 50% to detect landslide candidates as much as possible. But most falsely detected landslides can be removed with ensued joint analysis guided by landslide susceptibility. Thus, it can be concluded that the PA-TTA and the susceptibility guidance strategy are interdependent and indispensable. Without PA-TTA, applying the susceptibility guidance strategy would result in a low recall rate. Without the susceptibility guidance, applying the PA-TTA would not achieve high precision.

C. Effectiveness of Combining SG-FCNN With MCMO

As discussed above, the original SG-FCNN can detect all landslides (both historical and newly occurred landslides) from single temporal DAPs with high precision. To further expand the application scope of the SG-FCNN, an unsupervised change detection strategy MCMO was proposed to detect newly occurred landslides from bitemporal DAPs. As shown in Tables II and III, after integrating with the proposed MCMO strategy, the SG-FCNN achieved significantly higher accuracy in detecting newly occurred landslides than the original SG-FCNN. The result is especially obvious in testing region B, where the F_1 Score and IoU increased by 0.07 and 10.22%, reaching 0.8638 and 76.03%, respectively. The detection accuracy of testing region A is much higher, with an F_1 Score of 0.9169 and IoU of 84.65%, but the accuracy only increased by 0.012 and 2.02%, respectively. As shown in Figs. 17(c) and 18(c), the SG-FCNN successfully identified newly occurred landslides from all landslides with the help of the proposed MCMO. Especially in testing region B, numerous falsely detected landslides from a single temporal image, such as stony creeks [FP-B15 to FP-B18 in Fig. 14(i)], bare rocks [FP-B21 in Fig. 14(i)] and muddy tracks [FP-B21 in Fig. 14(i)] has also been identified as unchanged objects and removed. Compared to testing region B, the land-cover composition in testing region A is relatively simple, and the visual characteristics of landslides are clear and distinguishable. Thus, the detection result of all landslides

by the SG-FCNN in testing region A is already satisfactory, and the number of falsely detected landslides is scarce. This also explains why the accuracy increase in testing region A is lower than in testing region B after applying the proposed MCMO strategy.

In this article, the proposed MCMO was compared with the state-of-the-art change detection strategy of the CDCNN developed by Shi et al. [51]. As presented in Tables II, III, Figs. 17(b), and 18(b), the change detection strategy of the CDCNN has achieved a certain effect. Almost all historical landslides were identified and removed from the detection results of the SG-FCNN. In comparison, the proposed MCMO strategy is more effective with much higher accuracy in the two testing regions. The MCMO performs better as all unchanged land cover features, including historical landslides, can be identified and removed. In contrast, the change detection strategy of the CDCNN only identified and removed historical landslides but ignored other unchanged land cover features [FP-A12 to FP-A16 in Fig. 17(b), FP-B22 to FP-B26 in Fig. 18(b)]. In testing region B, some newly occurred landslides were misidentified as historical landslides and removed by the change detection strategy of the CDCNN [see FP-B27 and FP-B28 in Fig. 18(b)]. In addition, applying the MCMO strategy only need to calculate the mean changing magnitude of detected landslides based on CMI with a simple operation, and the whole processing time is less than a second. In contrast, the change detection strategy of the CDCNN needs to carry out an additional landslide detection process of prelandslide images using the SG-FCNN or FCNN, which significantly increases the processing time and computation burden. Thus, the MCMO strategy is much more efficient and easier to implement.

Given the above, with the help of the proposed MCMO, the proposed SG-FCNN has better accuracy and efficiency in detecting newly occurred landslides.

D. Defects of Proposed Landslide Detection Method

Despite the advantages of the proposed SG-FCNN and MCMO, false and misdetection of landslides cannot be avoided completely. A small number of muddy tracks, stony creeks, and other surface exposures not caused by landslides [FP-A4 to FP-A11 in Fig. 13(i), FP-B15 to FP-B21 in Fig. 14(i)] were falsely detected using the SG-FCNN due to the lack of assorted negative samples. In addition, the proposed method failed to detect those small landslides with a large length–width ratio because it is difficult to distinguish them from narrow roads based only on visual features [TP-A1 to TP-A4 in Fig. 13(a), TP-B1 to TP-B4 in Fig. 14(a)]. Although the proposed MCMO strategy can identify most of the falsely detected landslides as unchanged land cover features and then discard them, the others were still falsely detected because of the coregistration error of bitemporal images away from the isocenter [FP-A17 in Fig. 17(c)] and surface changes not caused by landslides [FP-A18 in Fig. 17(c), FP-B29 and FP-B30 in Fig. 18(c)]. Meanwhile, a small amount of newly occurred landslides were falsely identified as unchanged objects and removed [TP-B8 and TP-B9 in Fig. 18(a)] because their spectral characteristics

were not changed significantly. Introducing nonoptical remote sensing products and high-level feature extractions methods on a multiscale should be considered in future research.

Besides, the proposed SG-FCNN would result in additional time cost and parameter amount compared with the FCNN. The PA-TTA strategy requires the FCNN to detect the landslides multiple times. Thus, the additional time cost caused is obvious. The specific time cost depends on the number of applied data augmentation methods. In contrast, the PA-TTA strategy will not introduce new parameters. As for the SG strategy, the additional cost and parameter amount depend on the complexity of the applied landslide susceptibility mapping model. We will try to further improve the efficiency of the SG-FCNN by utilizing more efficient data-augmentation methods and landslide susceptibility model in our future article.

In addition, although the applied CPCNN-RF has achieved the best performance in Lantau Island, the generated landslide susceptibility map still could not guarantee 100% accuracy of landslide occurrence. The errors of the landslide susceptibility mapping would be transferred to landslide detection in the proposed SG-FCNN. Thus, it is equally important to study how to improve the reliability of landslide susceptibility mapping and reduce the negative impact caused by error transmission in our future article. Furthermore, limited by the quality of the data source, the spatial resolution of the landslide susceptibility map generated by the CPCNN-RF is only 30 m, which is inconsistent with the spatial resolution of DAPs. Applying a fine-grained landslide susceptibility map is a promising direction for minimizing the error caused by data scaling and improving the detection performance further.

VI. Conclusion

This article took a high-incidence area of landslide in Lantau Island as the study area and researched FCNN-based landslide detection method. First, various algorithm optimization methods such as overlapping mosaic detection strategy, compound loss function, and dense CRF were applied, which improved the detection accuracy of FCNN toward landslides' boundary. Based on this, the SG-FCNN was proposed to detect landslides under the guidance of landslide susceptibility. Through the analysis of experimental results, it can be concluded that the proposed landslide susceptibility guidance strategy has shown great potential in detecting landslides. By introducing landslide susceptibility as prior knowledge, the proposed SG-FCNN significantly outperforms the FCNN and the state-of-the-art post-processing method based on auxiliary information, with fewer false detection. Besides, an unsupervised change detection strategy, MCMO, was proposed and integrated with the SG-FCNN to detect newly occurred landslides based on bitemporal VHR remote sensing images. The proposed MCMO strategy is easy to implement and superior to the state-of-the-art change detection technique in terms of detection accuracy and efficiency. Applying the MCMO can fully utilize the merits of the unsupervised change detection strategy and the proposed SG-FCNN.

Given the above, the proposed SG-FCNN and MCMO strategy raises the performance of landslide detection to a new level

but also presents a new methodology for landslide detection by introducing landslide susceptibility as knowledge guidance, which is considered more important. The application range of landslide susceptibility maps would not be limited to landslide risk management and can be adopted in landslide inventory mapping. Considering that this is the first attempt to integrate landslide susceptibility and detection, this article also has a certain insufficiency as discussed in Section V-D, which should be addressed in our future article.

References

[1] X. Deng, D. Xu, M. Zeng, and Y. Qi, "Landslides and cropland abandonment in China's mountainous areas: Spatial distribution, empirical analysis and policy implications," *Sustainability*, vol. 10, no. 11, 2018, Art. no. 3909.

[2] C. L. H. Lam, J. W. C. Lau, and H. W. Chan, "Factual report on Hong Kong rainfall and landslides in 2008," Geotech. Eng. Office, Hong Kong, GEO Report No. 273, 2009.

[3] B.-G. Chae, H.-J. Park, F. Catani, A. Simoni, and M. Berti, "Landslide prediction, monitoring and early warning: A concise review of state-of-the-art," *Geosci. J.*, vol. 21, no. 6, pp. 1033–1070, 2017.

[4] M. Galli, F. Ardizzone, M. Cardinali, F. Guzzetti, and P. Reichenbach, "Comparing landslide inventory maps," *Geomorphology*, vol. 94, no. 3/4, pp. 268–289, 2008.

[5] C. J. Van Westen, E. Castellanos, and S. L. Kuriakose, "Spatial data for landslide susceptibility, hazard, and vulnerability assessment: An overview," *Eng. Geol.*, vol. 102, no. 3/4, pp. 112–131, 2008.

[6] F. Guzzetti, A. C. Mondini, M. Cardinali, F. Fiorucci, M. Santangelo, and K.-T. Chang, "Landslide inventory maps: New tools for an old problem," *Earth-Sci. Rev.*, vol. 112, no. 1-2, pp. 42–66, 2012.

[7] C. Van Westen, T. W. Van Asch, and R. Soeters, "Landslide hazard and risk zonation—Why is it still so difficult?," *Bull. Eng. Geol. Environ.*, vol. 65, no. 2, pp. 167–184, 2006.

[8] D. Brunsden, "Landslide types, mechanisms, recognition, identification," Landslides in the South Wales Coalfield, Edited by: Morgan, CS, 1985, pp. 1–3.

[9] A. Xing et al., "Dynamic analysis and field investigation of a fluidized landslide in Guanling, Guizhou, China," *Eng. Geol.*, vol. 181, pp. 1–14, 2014.

[10] G. Metternicht, L. Hurni, and R. Gogu, "Remote sensing of landslides: An analysis of the potential contribution to geo-spatial systems for hazard assessment in mountainous environments," *Remote Sens. Environ.*, vol. 98, no. 2/3, pp. 284–303, 2005.

[11] J. E. Nichol, A. Shaker, and M.-S. Wong, "Application of high-resolution stereo satellite images to detailed landslide hazard assessment," *Geomorphology*, vol. 76, no. 1/2, pp. 68–75, 2006.

[12] X. X. Zhu et al., "Deep learning in remote sensing: A comprehensive review and list of resources," *IEEE Geosci. Remote Sens. Mag.*, vol. 5, no. 4, pp. 8–36, Dec. 2017.

[13] F. Catani, "Landslide detection by deep learning of non-nadiral and crowd-sourced optical images," *Landslides*, vol. 18, no. 3, pp. 1025–1044, 2021.

[14] Z. Li, W. Shi, P. Lu, L. Yan, Q. Wang, and Z. Miao, "Landslide mapping from aerial photographs using change detection-based Markov random field," *Remote Sens. Environ.*, vol. 187, pp. 76–90, 2016, doi: 10.1016/j.rse.2016.10.008.

[15] J. G. Speight, "Landform pattern description from aerial photographs," *Photogrammetria*, vol. 32, no. 5, pp. 161–182, 1977.

[16] H. Cai, T. Chen, R. Niu, and A. Plaza, "Landslide detection using densely connected convolutional networks and environmental conditions," *IEEE J. Sel. Topics Appl. Earth Observ. Remote Sens.*, vol. 14, pp. 5235–5247, May 2021.

[17] G. Danneels, E. Pirard, and H.-B. Havenith, "Automatic landslide detection from remote sensing images using supervised classification methods," in *Proc. IEEE Int. Geosci. Remote Sens. Symp.*, 2007, pp. 3014–3017.

[18] V. Moosavi, A. Talebi, and B. Shirmohammadi, "Producing a landslide inventory map using pixel-based and object-oriented approaches optimized by Taguchi method," *Geomorphology*, vol. 204, pp. 646–656, 2014.

[19] D. T. Bui et al., "Landslide detection and susceptibility mapping by airsar data using support vector machine and index of entropy models in Cameron highlands, Malaysia," *Remote Sens.*, vol. 10, no. 10, 2018, Art. no. 1527.

[20] A. Stumpf and N. Kerle, "Object-oriented mapping of landslides using random forests," *Remote Sens. Environ.*, vol. 115, no. 10, pp. 2564–2577, 2011.

[21] W. Zhao and S. Du, "Learning multiscale and deep representations for classifying remotely sensed imagery," *ISPRS J. Photogramm. Remote Sens.*, vol. 113, pp. 155–165, 2016.

[22] C. Zhong et al., "Landslide mapping with remote sensing: Challenges and opportunities," *Int. J. Remote Sens.*, vol. 41, no. 4, pp. 1555–1581, 2020.

[23] L. Wan, T. Chen, A. Plaza, and H. Cai, "Hyperspectral unmixing based on spectral and sparse deep convolutional neural networks," *IEEE J. Sel. Topics Appl. Earth Observ. Remote Sens.*, vol. 14, pp. 11669–11682, Nov. 2021.

[24] H. Larochelle, Y. Bengio, J. Louradour, and P. Lamblin, "Exploring strategies for training deep neural networks," *J. Mach. Learn. Res.*, vol. 10, pp. 1–40, 2009.

[25] W. Zhou, Z. Shao, and Q. Cheng, "Deep feature representations for high-resolution remote sensing scene classification," in *Proc. 4th Int. Workshop Earth Observ. Remote Sens. Appl.*, 2016, pp. 338–342.

[26] Y. Chen, D. Ming, and X. Lv, "Superpixel based land cover classification of VHR satellite image combining multi-scale CNN and scale parameter estimation," *Earth Sci. Inform.*, vol. 12, no. 3, pp. 341–363, 2019.

[27] D. He, Q. Shi, X. Liu, Y. Zhong, and X. Zhang, "Deep subpixel mapping based on semantic information modulated network for urban land use mapping," *IEEE Trans. Geosci. Remote Sens.*, vol. 59, no. 12, pp. 10628–10646, Dec. 2021.

[28] X. Li, M. He, H. Li, and H. Shen, "A combined loss-based multiscale fully convolutional network for high-resolution remote sensing image change detection," *IEEE Geosci. Remote Sens. Lett.*, vol. 19, Jan. 2022, Art. no. 8017505.

[29] Q. Shi, M. Liu, S. Li, X. Liu, F. Wang, and L. Zhang, "A deeply supervised attention metric-based network and an open aerial image dataset for remote sensing change detection," *IEEE Trans. Geosci. Remote Sens.*, vol. 60, 2021, Art. no. 5604816.

[30] W. Wu et al., "Application of local fully convolutional neural network combined with YOLO v5 algorithm in small target detection of remote sensing image," *PLoS One*, vol. 16, no. 10, 2021, Art. no. e0259283.

[31] Y. Chen, D. Ming, X. Ling, X. Lv, and C. Zhou, "Landslide susceptibility mapping using feature fusion-based CPCNN-ML in Lantau Island, Hong Kong," *IEEE J. Sel. Topics Appl. Earth Observ. Remote Sens.*, vol. 14, pp. 3625–3639, Apr. 2021.

[32] L. Lv, T. Chen, J. Dou, and A. Plaza, "A hybrid ensemble-based deep-learning framework for landslide susceptibility mapping," *Int. J. Appl. Earth Observ. Geo-Inf.*, vol. 108, 2022, Art. no. 102713.

[33] Z. Ma, G. Mei, E. Prezioso, Z. Zhang, and N. Xu, "A deep learning approach using graph convolutional networks for slope deformation prediction based on time-series displacement data," *Neural Comput. Appl.*, vol. 33, no. 21, pp. 14441–14457, 2021.

[34] Q. Meng, H. Wang, M. He, J. Gu, J. Qi, and L. Yang, "Displacement prediction of water-induced landslides using a recurrent deep learning model," *Eur. J. Environ. Civil Eng.*, pp. 1–15, 2020.

[35] O. Ghorbanzadeh, A. Crivellari, P. Ghamisi, H. Shahabi, and T. Blaschke, "A comprehensive transferability evaluation of U-Net and ResU-Net for landslide detection from sentinel-2 data (case study areas from Taiwan, China, and Japan)," *Sci. Rep.*, vol. 11, no. 1, Jul. 2021, Art. no. 14629, doi: 10.1038/s41598-021-94190-9.

[36] H. Yu, Y. Ma, L. Wang, Y. Zhai, and X. Wang, "A landslide intelligent detection method based on CNN and RSG_R," in *Proc. IEEE Int. Conf. Mechatron. Automat.*, 2017, pp. 40–44.

[37] O. Ghorbanzadeh, T. Blaschke, K. Gholamnia, S. R. Meena, D. Tiede, and J. Aryal, "Evaluation of different machine learning methods and deep-learning convolutional neural networks for landslide detection," *Remote Sens.*, vol. 11, no. 2, 2019, Art. no. 196.

[38] M. I. Sameen and B. Pradhan, "Landslide detection using residual networks and the fusion of spectral and topographic information," *IEEE Access*, vol. 7, pp. 114363–114373, 2019.

[39] S. Ji, D. Yu, C. Shen, W. Li, and Q. Xu, "Landslide detection from an open satellite imagery and digital elevation model dataset using attention boosted convolutional neural networks," *Landslides*, vol. 17, no. 6, pp. 1337–1352, 2020.

[40] L. Bragagnolo, L. R. Rezende, R. V. da Silva, and J. M. V. Grzy-bowski, "Convolutional neural networks applied to semantic segmentation of landslide scars," *Catena*, vol. 201, 2021, Art. no. 105189, doi: 10.1016/j.catena.2021.105189.

[41] S. R. Meena et al., "Landslide detection in the Himalayas using machine learning algorithms and U-Net," *Landslides*, vol. 19, no. 5, pp. 1209–1229, 2022.

[42] N. Prakash, A. Manconi, and S. Loew, "Mapping landslides on EO data: Performance of deep learning models vs. traditional machine learning models," *Remote Sens.*, vol. 12, no. 3, 2020, Art. no. 346.

[43] P. Liu, Y. Wei, Q. Wang, Y. Chen, and J. Xie, "Research on post-earthquake landslide extraction algorithm based on improved u-net model," *Remote Sens.*, vol. 12, no. 5, 2020, Art. no. 894.

[44] O. Ghorbanzadeh, K. Gholamnia, and P. Ghamisi, "The application of ResU-Net and OBIA for landslide detection from multi-temporal sentinel-2 images," *Big Earth Data*, pp. 1–26, 2022.

[45] P. Liu et al., "A research on landslides automatic extraction model based on the improved mask R-CNN," *ISPRS Int. J. Geo-Inf.*, vol. 10, no. 3, 2021, Art. no. 168.

[46] O. Ghorbanzadeh, S. R. Meena, H. S. S. Abadi, S. T. Piralilou, L. Zhiyong, and T. Blaschke, "Landslide mapping using two main deep-learning convolution neural network streams combined by the Dempster–Shafer model," *IEEE J. Sel. Topics Appl. Earth Observ. Remote Sens.*, vol. 14, pp. 452–463, Jan. 2021.

[47] T. Lei, Y. Zhang, Z. Lv, S. Li, S. Liu, and A. K. Nandi, "Landslide inventory mapping from bitemporal images using deep convolutional neural networks," *IEEE Geosci. Remote Sens. Lett.*, vol. 16, no. 6, pp. 982–986, Jun. 2019.

[48] X. Gao, T. Chen, R. Niu, and A. Plaza, "Recognition and mapping of landslide using a fully convolutional DenseNet and influencing factors," *IEEE J. Sel. Topics Appl. Earth Observ. Remote Sens.*, vol. 14, pp. 7881–7894, Aug. 2021.

[49] T. Liu, T. Chen, R. Niu, and A. Plaza, "Landslide detection mapping employing CNN, ResNet, and DenseNet in the Three Gorges Reservoir, China," *IEEE J. Sel. Topics Appl. Earth Observ. Remote Sens.*, vol. 14, pp. 11417–11428, Nov. 2021.

[50] O. Ghorbanzadeh, H. Shahabi, A. Crivellari, S. Homayouni, T. Blaschke, and P. Ghamisi, "Landslide detection using deep learning and object-based image analysis," *Landslides*, vol. 19, no. 4, pp. 929–939, 2022.

[51] W. Shi, M. Zhang, H. Ke, X. Fang, Z. Zhan, and S. Chen, "Landslide recognition by deep convolutional neural network and change detection," *IEEE Trans. Geosci. Remote Sens.*, vol. 59, no. 6, pp. 4654–4672, Jun. 2021.

[52] K. S. Cheng, C. Wei, and S. Chang, "Locating landslides using multi-temporal satellite images," *Adv. Space Res.*, vol. 33, no. 3, pp. 296–301, 2004.

[53] D. Wen et al., "Change detection from very-high-spatial-resolution optical remote sensing images: Methods, applications, and future directions," *IEEE Geosci. Remote Sens. Mag.*, vol. 9, no. 4, pp. 68–101, Dec. 2021, doi: 10.1109/mgrs.2021.3063465.

[54] P. Reichenbach, M. Rossi, B. D. Malamud, M. Mihir, and F. Guzzetti, "A review of statistically-based landslide susceptibility models," *Earth-Sci. Rev.*, vol. 180, pp. 60–91, 2018.

[55] F. Guzzetti, "Landslide hazard and risk assessment," Ph.D. dissertation, Univ. Bonn (Rheinische Friedrich-Wilhelms-Universität Bonn), Bonn, Germany, 2006.

[56] R. Langford, J. James, R. Shaw, S. Campbell, P. Kirk, and R. Sewell, *Geology of Lantau District*, vol. 6. Hong Kong: Geotechnical Eng. Office Hong Kong Government, 1995.

[57] "Climate change and extreme landslide events," G. E. Office, 2021.

[58] Z. Su, J. K. Chow, P. S. Tan, J. Wu, Y. K. Ho, and Y.-H. Wang, "Deep convolutional neural network–based pixel-wise landslide inventory mapping," *Landslides*, vol. 18, no. 4, pp. 1421–1443, 2021.

[59] M.-F. J. Venture, "Final report on compilation of the enhanced natural terrain landslide inventory (ENTLI)," Maunsell-Fugro Joint Venture and Geotechnical Engineering Office, Hong Kong, 2007.

[60] O. Ronneberger, P. Fischer, and T. Brox, "U-net: Convolutional networks for biomedical image segmentation," in *Proc. Int. Conf. Med. Image Comput. Comput.-Assisted Intervention*, 2015, pp. 234–241.

[61] M. Sandler, A. Howard, M. Zhu, A. Zhmoginov, and L.-C. Chen, "Mobilenetv2: Inverted residuals and linear bottlenecks," in *Proc. IEEE Conf. Comput. Vis. Pattern Recognit.*, 2018, pp. 4510–4520.

[62] A. Odena, V. Dumoulin, and C. Olah, "Deconvolution and checkerboard artifacts," 2016. [Online]. Available: https://distill.pub/2016/deconv-checkerboard/

[63] F. Milletari, N. Navab, and S.-A. Ahmadi, "V-net: Fully convolutional neural networks for volumetric medical image segmentation," in *Proc. 4th Int. Conf. 3D Vis.*, 2016, pp. 565–571.

[64] Y. Ho and S. Wookey, "The real-world-weight cross-entropy loss function: Modeling the costs of mislabeling," *IEEE Access*, vol. 8, pp. 4806–4813, 2020.

[65] E. W. Weisstein, "Moore neighborhood," *From MathWorld–A Wolfram Web Resource*, 2005. [Online]. Available: http://mathworld.wolfram.com/MooreNeighborhood.html

[66] E. E. Brabb, "Innovative approaches to landslide hazard and risk mapping," in *Proc. Int. Landslide Symp.*, 1985, pp. 17–22.

[67] S. D. Pardeshi, S. E. Autade, and S. S. Pardeshi, "Landslide hazard assessment: Recent trends and techniques," *Springer Plus*, vol. 2, no. 1, pp. 1–11, 2013.

[68] Y. Wang, Z. Fang, and H. Hong, "Comparison of convolutional neural networks for landslide susceptibility mapping in Yanshan County, China," *Sci. Total Environ.*, vol. 666, pp. 975–993, 2019.

[69] Z. Fang, Y. Wang, L. Peng, and H. Hong, "Integration of convolutional neural network and conventional machine learning classifiers for landslide susceptibility mapping," *Comput. Geosci.*, vol. 139, 2020, Art. no. 104470.

[70] H. Wang, L. Zhang, H. Luo, J. He, and R. Cheung, "AI-powered landslide susceptibility assessment in Hong Kong," *Eng. Geol.*, vol. 288, 2021, Art. no. 106103.

[71] P. Krähenbühl and V. Koltun, "Efficient inference in fully connected CRFs with Gaussian edge potentials," *Adv. Neural Inf. Process. Syst.*, vol. 24, pp. 109–117, 2011.

[72] J. Shotton, J. Winn, C. Rother, and A. Criminisi, "Textonboost for image understanding: Multi-class object recognition and segmentation by jointly modeling texture, layout, and context," *Int. J. Comput. Vis.*, vol. 81, no. 1, pp. 2–23, 2009.

[73] P. Soille, *Morphological Image Analysis: Principles and Applications*. Berlin, Germany: Springer-Verlag, 1999.

[74] Z. Li, W. Shi, S. W. Myint, P. Lu, and Q. Wang, "Semi-automated landslide inventory mapping from bitemporal aerial photographs using change detection and level set method," *Remote Sens. Environ.*, vol. 175, pp. 215–230, 2016.

[75] Z. Y. Lv, W. Shi, X. Zhang, and J. A. Benediktsson, "Landslide inventory mapping from bitemporal high-resolution remote sensing images using change detection and multiscale segmentation," *IEEE J. Sel. Topics Appl. Earth Observ. Remote Sens.*, vol. 11, no. 5, pp. 1520–1532, May 2018.

[76] P. Gong et al., "Finer resolution observation and monitoring of global land cover: First mapping results with Landsat TM and ETM+ data," *Int. J. Remote Sens.*, vol. 34, no. 7, pp. 2607–2654, 2013.

Dongping Ming (Member, IEEE) received the B.E. degree in land administration and cadastral surveying from the Wuhan Technical University of Surveying and Mapping, Wuhan, China, in 1999, the M.E. degree in cartography and geographic information engineering from the Wuhan University, Wuhan, China, in 2002, and the Ph.D. degree in cartography and geographic information system from the Institute of Geographical Sciences and Natural Resources Research, Chinese Academy of Sciences, Beijing, China, in 2006.

She is currently a Professor with the School of Information Engineering, China University of Geosciences, Beijing. Her research interests include remote-sensing image processing and analysis, information extraction from high spatial resolution satellite remote sensing images, and spatial statistics and its application.

Junchuan Yu received the Ph.D. degree in mineralogy, petrology, mineral deposit geology from the China University of Geosciences, Beijing, China, in 2013.

He is currently working with the Department of Satellite Application Research, China Aero Geophysical Survey and Remote Sensing Center for Natural Resources, Beijing, China. His research interests include hyperspectral remote sensing, deep learning, and geological application.

Lu Xu received the B.S. degree in geographical information science from the China University of Geosciences, Beijing, China, in 2018. He is currently working toward the Ph.D. degree in surveying and mapping with the China University of Geosciences.

His research interests include theory of object-based image analysis and image information extraction by deep-learning methods.

Yangyang Chen was born in Beijing, China, in 1992. He received the B.S. degree in geographic information science, the M.E. degree in surveying and mapping engineering, and the Ph.D. degree in surveying and mapping from the China University of Geosciences, Beijing, China, in 2015, 2018, and 2022, respectively.

He is currently an Engineer with the China Aero Geophysical Survey and Remote Sensing Center for Natural Resources, Beijing, China. His research interests include high spatial resolution remote sensing image processing and analysis, landslide information extraction, and semantic understanding of urban functional zone.

Yanni Ma received the B.S. degree in geographical information science in 2014 and the M.S. degree in surveying and mapping in 2018 from the China University of Geosciences, Beijing, China. She is currently working toward the Ph.D. degree in surveying and mapping with the China University of Geosciences.

She is currently an Engineer with the China Aero Geophysical Survey and Remote Sensing Center for Natural Resources. Her research interests include remote-sensing image analysis and deep-learning application.

Yan Li received the B.S. degree in geographical information science from the China University of Geosciences, Beijing, China, in 2020. She is currently working toward the Ph.D. degree in surveying and mapping with the China University of Geosciences, Beijing, China.

　　Her research interests include high-resolution remote sensing image procession and landslide risk evaluation.

Yueqin Zhu received the Ph.D. degree in cartography from the Technical University of Munich, Munich, Germany, in 2012.

　　She is currently a Senior Engineer with the National Institute of Natural Hazards, Ministry of Emergency Management, Beijing, China. Her research interests include cloud computing, computational intelligence, and cartography.

Xiao Ling received the B.S. degree in geomatic engineering from the Nanjing Normal University, Nanjing, China, in 2017, and the M.E. degree in surveying and mapping engineering from the China University of Geosciences, Beijing, China, in 2021. She is currently working toward the Ph.D. degree in surveying and mapping with the China University of Geosciences.

　　Her research interests include landslide hazard, susceptibility analysis, and high-resolution remote sensing image procession.